

# On the Electron Pairing Mechanism of Copper-Oxide High Temperature Superconductivity

S.M. O'Mahony<sup>1§</sup>, Wangping Ren<sup>2§</sup>, Weijiong Chen<sup>2</sup>, Yi Xue Chong<sup>3</sup>, Xiaolong Liu<sup>3,4</sup>,  
H. Eisaki<sup>5</sup>, S. Uchida<sup>6</sup>, M.H. Hamidian<sup>3</sup>, and J.C. Séamus Davis<sup>1,2,3,7</sup>

1. Department of Physics, University College Cork, Cork T12 R5C, Ireland
  2. Clarendon Laboratory, University of Oxford, Oxford, OX1 3PU, UK.
  3. Department of Physics, Cornell University, Ithaca NY 14850, USA
  4. Kavli Institute for Nanoscale Science, Cornell University, Ithaca, NY 14853, USA
  5. Inst. of Advanced Industrial Science and Tech., Tsukuba, Ibaraki 305-8568, Japan.
  6. Department of Physics, University of Tokyo, Bunkyo, Tokyo 113-0011, Japan.
  7. Max-Planck Institute for Chemical Physics of Solids, D-01187 Dresden, Germany
- § These authors contributed equally to this project.

**ABSTRACT** The elementary  $\text{CuO}_2$  plane sustaining cuprate high temperature superconductivity<sup>1</sup> occurs typically at the base of a periodic array of edge-sharing  $\text{CuO}_5$  pyramids (Fig 1a). Virtual transitions of electrons between adjacent planar Cu and O atoms, occurring at a rate  $t/\hbar$  and across the charge-transfer<sup>2</sup> energy gap  $\mathcal{E}$ , generate ‘superexchange’ spin-spin interactions<sup>3,4</sup> of energy  $J \approx 4t^4/\mathcal{E}^3$  in an antiferromagnetic correlated-insulator state<sup>1</sup>. Hole doping the  $\text{CuO}_2$  plane disrupts this magnetic order while perhaps retaining superexchange interactions, thus motivating an hypothesis of spin-singlet electron-pair formation at energy scale  $J$  as the mechanism of high temperature superconductivity<sup>5</sup>. Although the response of the superconductor’s electron-pair wavefunction  $\Psi \equiv \langle c_{\uparrow}c_{\downarrow} \rangle$  to alterations in  $\mathcal{E}$  should provide a direct test of such hypotheses, measurements have proven impracticable. Focus has turned instead to the distance  $\delta$  between each Cu atom and the O atom at the apex of its  $\text{CuO}_5$  pyramid. Varying  $\delta$  should alter the Coulomb potential at the planar Cu and O atoms, modifying  $\mathcal{E}$  and thus  $J$ , and thereby controlling  $\Psi$  in a predictable manner<sup>6,7,8,9,10,11</sup>. Here we implement atomic-scale imaging of  $\mathcal{E}$  and  $\Psi$ , both as a function of the periodic modulation in  $\delta$  that occurs naturally in  $\text{Bi}_2\text{Sr}_2\text{CaCu}_2\text{O}_{8+\delta}$ . We demonstrate that the responses of  $\mathcal{E}$  and  $\Psi$  to varying  $\delta$ , and crucially those of  $\Psi$  to the varying  $\mathcal{E}$ , conform to theoretical predictions<sup>7,8,9,10</sup>. These data provide direct atomic-scale verification that charge-transfer superexchange is key to the electron-pairing mechanism in the hole-doped cuprate superconductor  $\text{Bi}_2\text{Sr}_2\text{CaCu}_2\text{O}_{8+x}$ .

In transition-metal oxide insulators, superexchange<sup>3</sup> generates intense magnetic interactions between electrons that are localized at adjacent transition-metal atoms, typically generating robust antiferromagnetism. The superexchange interaction occurs when the degeneracy of transition-metal  $3d$  orbitals is lifted by the Coulomb energy  $U$  required for their double occupancy, so that intervening oxygen  $2p$  energy levels are separated from the relevant transition-metal  $3d$  level by the charge-transfer energy  $\mathcal{E}$  (Fig. 1a). In this case, interactions of two adjacent  $3d$  electrons of spin  $\mathbf{S}_i$  are well approximated by a Heisenberg Hamiltonian  $H = J\mathbf{S}_i \cdot \mathbf{S}_j$ , where  $J \approx 4t^4/\mathcal{E}^3$  and  $t/\hbar$  is the transition rate of between  $3d$  and  $2p$  orbitals (Fig. 1a). In the  $\text{CuO}_2$ -based materials<sup>1</sup> the planar  $\text{Cu}^{2+}$  ions are in the  $3d^9$  configuration with a singly occupied  $d_{x^2-y^2}$  orbital, while the planar  $\text{O}^{2-}$  ions have closed  $2p^6$  shells whose in-plane  $p_\sigma$  orbitals dominate. To doubly occupy any  $d_{x^2-y^2}$  orbital requires an energy  $U$  so great that the  $d$ -electrons become fully Mott-localized in a charge-transfer insulator<sup>2</sup> state, with the  $p_\sigma$  energy level separated from the pertinent  $d_{x^2-y^2}$  level by the  $\text{CuO}_2$  charge-transfer energy  $\mathcal{E}$  (Fig. 1a). Under such circumstances, an electronic structure with  $t \approx 0.4$  eV and  $\mathcal{E} \approx 1$  eV implies a superexchange energy  $J \approx 100$  meV that should stabilize a robust spin-1/2,  $\mathbf{Q} = (\pi, \pi)$  antiferromagnetic state (Fig. 1b). Just such a state is observed<sup>1,12</sup>.

However, when holes are doped into the  $\text{CuO}_2$ -plane they enter the  $p_\sigma$  orbitals, both disrupting the antiferromagnetic order and delocalizing the electrons within an intensely correlated yet metallic band structure<sup>6,7,10,11</sup> that still retains a charge-transfer energy scale  $\mathcal{E}$  (Fig. 1c). This situation may be approximated using the Hubbard<sup>13,14</sup> Hamiltonian:  $H = \sum_{ij,\sigma} t_{ij}^d c_{i\sigma}^{\dagger d} c_{j\sigma}^d + U \sum_{i\sigma} n_{i\uparrow}^d n_{i\downarrow}^d$  where  $t_{ij}^d/\hbar$  is the electron hopping-rate between  $d$ -orbitals at adjacent planar sites  $i$  and  $j$ ,  $c_{i\sigma}^{\dagger d}$  ( $c_{i\sigma}^d$ ) creates(annihilates) an electron with spin-state  $\sigma$  at  $d$ -orbital  $i$ , and  $n_{i\sigma}^d \equiv c_{i\sigma}^{\dagger d} c_{i\sigma}^d$ . Heuristically, such models describe a two-dimensional correlated metallic state with intense antiferromagnetic spin-spin interactions. Superconductivity is then signified by the appearance of electron-pair wavefunction with amplitude  $\Psi \equiv \langle c_{i\downarrow}^d c_{j\uparrow}^d \rangle$ , a phenomenon recently made accessible to visualization using scanned Josephson tunneling microscopy<sup>15,16,17,18,19</sup>. For cuprates, the revolutionary hypothesis for the electron-pairing

mechanism of high-temperature superconductivity<sup>5,20,21,22,23,24,25,26,27</sup> was then for a spin-singlet superconductor where electron-electron interactions are mediated by superexchange, but whose electron-pair wavefunction  $\Psi$  is subject to the strong no-double-occupancy constraints on the Cu  $d_{x^2-y^2}$  orbitals<sup>28,29</sup> (Fig. 1c). When such interactions and constraints are studied using mean-field Gutzwiller projection<sup>21,22</sup>, or by slave-boson techniques<sup>23,24,25</sup>, or by Monte Carlo numerical techniques<sup>26,27</sup> the phase diagram and many other key characteristics that emerge are congruent with observations<sup>28,29</sup>. Moreover, current studies using dynamical mean-field theory (DMFT) find that it is indeed the superexchange interaction which creates electron pairing in the three band CuO<sub>2</sub> Hubbard model<sup>30,31,32,33,34,35,36</sup>. But despite enormous research efforts<sup>1</sup>, neither this nor any other theory for the electron pairing mechanism of cuprate superconductors has yet been established convincingly by experiment. Fundamentally, this is because techniques to directly and simultaneously measure  $\mathcal{E}$  and  $\Psi$ , and thus to determine their microscopic interplay, have proven elusive.

Lately, however, DMFT analysis of the CuO<sub>2</sub> Hubbard model<sup>6-10</sup> has yielded quantitative predictions of how the electron-pair wavefunction  $\Psi$  is controlled by  $\mathcal{E}$ , and how this interplay could be verified by altering the distance  $\delta$  between each Cu atom and the apical O atom of its CuO<sub>5</sub> pyramid<sup>7,8,9</sup>. For experimentalists, the consequent challenge was to measure the relationship between  $\Psi$  and  $\mathcal{E}$  directly and simultaneously at the superconducting CuO<sub>2</sub>-plane. Such data could play a role analogous to the *isotope effect* in conventional superconductors<sup>37</sup> by identifying empirically the specific electron-electron interaction that lowers energy upon electron pair formation. Studies of  $\mathcal{E}$  and  $J$  in cuprates have long been carried out using optical reflectivity, Raman spectroscopy tunneling spectroscopy, angle resolved photoemission, and resonant inelastic X-ray scattering (SI Section ‘Measuring Charge Transfer Energy, Superexchange and Superconductivity’). Typically, to access different  $\mathcal{E}$  for these studies required changing between crystal families in the antiferromagnetic-insulator state. But this renders impossible the required comparison between  $\mathcal{E}$  and  $\Psi$  measured simultaneously in the same superconductive state. Instead, the maximum superconducting critical temperature  $T_c$  subsequent to hole-doping

is often proposed as a proxy for  $\langle c_{\uparrow}c_{\downarrow} \rangle$  and then compared the  $\mathcal{E}$  derived from the parent insulator, for a range of different compounds. But varying the crystal family alters a wide variety of other material parameters besides  $\mathcal{E}$ , and  $T_c$  is anyway controlled by other influences including dimensionality and superfluid phase-stiffness<sup>38</sup>. More fundamentally, advanced analysis has recently revealed that, even in principle, a one-to-one correspondence does not exist<sup>10,11</sup> between the  $T_c$  and  $\Psi$  in the of the CuO<sub>2</sub> Hubbard model. Hence, although greatly encouraging, studies comparing maximum  $T_c$  with insulating  $\mathcal{E}$  cannot be conclusive as to the electron-pairing mechanism. Instead, a direct and systematic measurement of the dependence of the electron-pair wavefunction  $\Psi \equiv \langle c_{\uparrow}c_{\downarrow} \rangle$  on the charge-transfer energy  $\mathcal{E}$ , is required.

In theory<sup>7,8,9,39,40,41,42</sup>, a direct route to controlling  $\mathcal{E}$  in the CuO<sub>2</sub>-plane is to vary the distance  $\delta$  between the oxygen ion at the apex of each CuO<sub>5</sub> pyramid and the planar Cu atom beneath it (Fig 1a). More specifically, when cluster DMFT theory is used to predict the atomic-scale responses of both  $\mathcal{E}$  and  $\Psi$  to variations in  $\delta$  within the CuO<sub>5</sub> pyramid, the essential physics stressed is: *“as we bring the negatively charged apical oxygen towards the CuO plane, the resulting electrostatic repulsion ..... increases  $\mathcal{E}$  by rendering it costly to place an electron on the Cu site”*<sup>7</sup>. In such studies<sup>7-11</sup>, the Hubbard Hamiltonian utilizes a single Cu  $d_{x^2-y^2}$  and two O  $p_{\sigma}$  orbitals:

$$H = \sum_{i\alpha j\beta, \sigma} t_{ij}^{\alpha\beta} c_{i\sigma}^{\dagger\alpha} c_{j\sigma}^{\beta} + \sum_{i\sigma, \alpha} \varepsilon_{\alpha} n_{i\sigma}^{\alpha} + U \sum_{i\sigma} n_{i\uparrow}^d n_{i\downarrow}^d \quad (1)$$

where  $i, j$  enumerate planar CuO<sub>2</sub> unit cells,  $\alpha, \beta$  label any of the three orbitals,  $t_{ij}^{\alpha\beta}$  are transition rates for electrons between orbitals  $\alpha, \beta$  at sites  $i, j$ ,  $\varepsilon_{\alpha}$  are the orbital energies, and  $n_{i\uparrow}^d, n_{i\downarrow}^d$  are the  $d_{x^2-y^2}$  orbital occupancies by spin state. DMFT analysis of Eqn. 1 yields several key quantitative predictions<sup>7,8,9</sup> for effects on both the charge-transfer energy  $\mathcal{E}$  and the electron-pair wavefunction  $\Psi$ , of displacing the apical oxygen atom vertically by  $\delta$ . This represents an exciting new opportunity: measurement of the dependences of  $\mathcal{E}$  and  $\Psi$  at the Cu atom beneath each displaced apical oxygen atom could yield a quantitative knowledge of  $d\Psi/d\mathcal{E}$ , providing a direct test for a charge-transfer superexchange electron-pairing mechanism.



To explore this prospect, one must measure  $\mathcal{E}$  and  $\Psi$  as a function of the value of  $\delta$  above each planar Cu atom. But  $\Psi$  is a complex-valued field and thus not a physical observable, meaning that experiments must study  $|\Psi|^2 \equiv n_p$ , the electron-pair density. Our strategy then combines two novel techniques in atomic resolution imaging with a fortuitous property of the canonical cuprate  $\text{Bi}_2\text{Sr}_2\text{CaCu}_2\text{O}_{8+x}$ . First, a mismatch between preferred bond lengths of the rock-salt and perovskite layers in  $\text{Bi}_2\text{Sr}_2\text{CaCu}_2\text{O}_{8+\delta}$  generates a  $\sim 26\text{\AA}$ -periodic modulation of unit-cell dimensions (Fig. 1d), along the crystal  $a$ -axis or equivalently the (1,1) axis of the  $\text{CuO}_2$  plane<sup>43</sup>. Providentially, this *supermodulation* generates variations in  $\delta$  by up to 12%, this being the largest fractional change of any bond-length within the  $\text{CuO}_5$  pyramid. Crucially, the value of  $\delta$  at every location  $\mathbf{r}$  can be evaluated by atomic-resolution imaging of the supermodulation in topographic images  $T(\mathbf{r})$  measured at the crystal's BiO termination layer (Fig. 2a), and then by using X-ray crystallography to relate  $T(\mathbf{r})$  to the spatial pattern of apical displacements  $\delta(\mathbf{r})$  just underneath (SI Section ‘Supermodulation phase  $\Phi(\mathbf{r})$  and apical displacement  $\delta(\mathbf{r})$ ’). Second, by measuring differential tunnel conductance  $dI/dV(\mathbf{r}, V) \equiv g(\mathbf{r}, V)$  as a function of location  $\mathbf{r}$  and tip-sample voltage  $V$ , the density of electronic states  $N(\mathbf{r}, E) \propto g(\mathbf{r}, V = E/e)$  can be visualized for the high energy range governed by Eqn. 1. In principle, this allows energy scales such as  $\mathcal{E}(\mathbf{r})$  in the spectrum of  $\text{Bi}_2\text{Sr}_2\text{CaCu}_2\text{O}_{8+x}$  to be determined versus location  $\mathbf{r}$ . Third, using superconducting STM tips to image the Josephson critical current  $I_J$  for electron-pair tunneling versus location  $\mathbf{r}$ , allows direct visualization of sample's electron-pair density  $n_p(\mathbf{r}) \equiv |\Psi|^2 \propto (I_J(\mathbf{r})R_N(\mathbf{r}))^2$  where  $R_N$  is the tip-sample junction resistance. Thus, our concept is to visualize both  $\mathcal{E}(\mathbf{r})$  and  $n_p(\mathbf{r})$  directly at atomic scale, as a function of the apical oxygen displacements  $\delta(\mathbf{r})$  that are produced by the crystal supermodulation in  $\text{Bi}_2\text{Sr}_2\text{CaCu}_2\text{O}_{8+x}$ .

In practice, single crystals of  $\text{Bi}_2\text{Sr}_2\text{CaCu}_2\text{O}_{8+x}$  with hole-density  $p \approx 0.17$  are cleaved in cryogenic ultrahigh vacuum in a dilution refrigerator based spectroscopic imaging scanning tunnelling microscope (SISTM), to reveal the BiO termination layer (Fig. 2a). The  $\text{CuO}_2$  plane is  $\sim 5\text{\AA}$  beneath the BiO surface and separated from it by the SrO layer containing the apical oxygen atom of each  $\text{CuO}_5$  pyramid (Fig. 1c). A surface corrugation  $T(\mathbf{r}) =$

$A(\mathbf{r})\cos\Phi(\mathbf{r})$ , where  $\Phi(\mathbf{r}) = \mathbf{Q}_S \cdot \mathbf{r} + \theta(\mathbf{r})$ , occurs at the bulk supermodulation wavevector  $\mathbf{Q}_S \cong (0.15, 0.15)2\pi/a_0$  where  $\theta(\mathbf{r})$  describes effects of disorder (Fig. 2a). The supermodulation phase  $\Phi(\mathbf{r})$  is then imaged by analyzing  $T(\mathbf{q})$ , the Fourier transform of  $T(\mathbf{r})$ , with results shown in Fig. 2b (SI Section ‘Supermodulation phase  $\Phi(\mathbf{r})$  and apical displacement  $\delta(\mathbf{r})$ ’). X-ray scattering studies of the  $\text{Bi}_2\text{Sr}_2\text{CaCu}_2\text{O}_{8+x}$  crystal supermodulation demonstrate that the distance to apical oxygen atom  $\delta$  is minimal at  $\Phi = 0$  and maximal at  $\Phi = \pi$ , because the displacement amplitude of the  $c$ -axis supermodulation is greater in the  $\text{CuO}_2$  layer than in the adjacent  $\text{SrO}$  layer. Thus,  $\delta(\mathbf{r})$  is determined from the measured  $\Phi(\mathbf{r})$  based on X-ray refinement as:  $\delta(\Phi) \approx 2.44 - 0.14\cos(\Phi)$  Å (SI Section ‘Supermodulation phase  $\Phi(\mathbf{r})$  and apical displacement  $\delta(\mathbf{r})$ ’). For example, the apical displacement imaging results  $\delta(\mathbf{r})$  from Fig. 2a,b are shown in Fig. 2c. This same  $\Phi(\mathbf{r})$ : $\delta(\mathbf{r})$  procedure is used throughout our study.

Next, Figure 3a shows a typical  $g(V)$  spectrum measured at the  $\text{BiO}$  termination layer using  $R_N \approx 85$  G $\Omega$ . At this scale, the metallic density of states surrounding the Fermi energy is imperceptible, while the minimum energy difference between the lower and upper bands is obvious (double headed arrow Fig. 3a and SI Section ‘Charge transfer energy visualization  $\mathcal{E}(\mathbf{r})$  by SISTM’). One can determine empirically if  $\mathcal{E}(\mathbf{r})$  modulations exist, by visualizing both  $g(\mathbf{r}, V)$  in the  $-1.6 \text{ V} \leq V \leq 2 \text{ V}$  range, and  $\Phi(\mathbf{r})$  from the simultaneous  $T(\mathbf{r})$ . Then, by averaging all  $g(V)$  associated with each  $\Phi$ ,  $g(\Phi, V)$  is determined. Figure 3c shows measured  $g(\Phi, V)$  which manifests strong clear modulations of the energy separation between the band edges, at the wavevector  $\mathbf{Q}_S$ . Correspondingly, using SJTM with a tip terminating in a  $\text{Bi}_2\text{Sr}_2\text{CaCu}_2\text{O}_{8+x}$  nanoparticle<sup>17</sup> and  $R_N \approx 21$  M $\Omega$ , we find tip-sample Josephson junction exhibits a phase-diffusive<sup>17,18,19</sup> steady-state at voltage  $V_J$ , with electron-pair current  $I_P(V_J) = \frac{1}{2}I_J^2 Z V_J / (V_J^2 + V_C^2)$  where  $Z$  the high-frequency junction impedance and  $V_C$  is the voltage for maximum  $I_P(V_J)$ . A typical example of measured  $I_P(V_J)$  is shown in Fig. 3b. Then, because the maxima in  $I_P(V_J)$  occur at  $I_m \propto I_J^2$ , atomic-scale visualization of an electron-pair density is achieved<sup>15,16</sup> as  $n_P(\mathbf{r}) \propto I_m(\mathbf{r})R_N^2(\mathbf{r})$  or equivalently  $n_P(\mathbf{r}) \propto g_0(\mathbf{r})R_N^2(\mathbf{r})$  (SI Section ‘Electron-pair density visualization  $n_P(\mathbf{r})$  by SJTM’). Hence, one can determine empirically if  $n_P(\mathbf{r})$  modulations exist, by measuring  $I_P(\mathbf{r}, V_J)$  and  $\Phi(\mathbf{r})$  from the

simultaneous  $T(\mathbf{r})$ . Again, by averaging all values of  $|I_p(\mathbf{r}, V_I)|$  associated with each  $\Phi$ , the  $|I_p(\Phi, V_I)|$  is determined. The result, as shown in Fig. 3d, clearly demonstrates that  $I_M$  is also modulating at wavevector  $\mathbf{Q}_S$ . Together, these data represent empirical discovery that both the band-separation energy  $\mathcal{E}(\mathbf{r})$  and the electron-pair density  $n_p(\mathbf{r})$  are modulated periodically, by the crystal supermodulation of  $\text{Bi}_2\text{Sr}_2\text{CaCu}_2\text{O}_{8+x}$ .

To quantify and relate these phenomena, we consider two exemplary fields of view whose  $T(\mathbf{r})$  are shown Fig. 4a,b. Both  $T(\mathbf{r})$  images are evaluated to determine their separate  $\Phi(\mathbf{r})$ , with the ends of the  $\Phi = \pi$  contours indicated by the arrowheads in each. A high-voltage single-electron tunnelling  $g(\mathbf{r}, V)$  map is measured at  $R_N \approx 85 \text{ G}\Omega$  and  $T = 4.2 \text{ K}$  in the FOV of Fig. 4a, while a low-voltage electron-pair tunnelling  $I_p(V_I)$  map at  $R_N \approx 21 \text{ M}\Omega$  and  $T = 2 \text{ K}$  is measured in that of Fig. 4b. To visualize  $\mathcal{E}(\mathbf{r})$ , we estimate  $\mathcal{E}$  to be the minimum energy difference between upper and lower bands<sup>44</sup> at a constant conductance  $G \approx 20 \text{ pS}$ , as shown by double headed arrow. The resulting  $\mathcal{E}(\mathbf{r})$  shown in Fig. 4c is correctly representative and appears little different if we estimate  $\mathcal{E}(\mathbf{r})$  anywhere in the range  $20 \text{ pS} \leq G \leq 80 \text{ pS}$  (SI Section ‘Charge transfer energy visualization  $\mathcal{E}(\mathbf{r})$  by SISTM’). Concomitantly, to visualize  $n_p(\mathbf{r})$  we measure  $g_0(\mathbf{r})$  and multiply by the measured  $R_N^2(\mathbf{r})$  modulations from the same FOV as Fig. 4b (SI Section ‘Electron-pair density visualization  $n_p(\mathbf{r})$  by SJTM’). Thus, Fig. 4d shows measured  $n_p(\mathbf{r})$  in the FOV of Fig. 4b. Finally, when Fig. 4c is Fourier-filtered at  $\mathbf{Q}_S$  it reveals the first-harmonic modulations in  $\mathcal{E}(\mathbf{r})$  as presented in Fig. 4e, while similarly filtering of Fig. 4d at  $\mathbf{Q}_S$  yields the first-harmonic modulations in  $n_p(\mathbf{r})$  as seen in Fig. 4f. Thus, visualization of the crystal supermodulation effect on both  $\mathcal{E}(\mathbf{r})$  and  $n_p(\mathbf{r})$ , simultaneously with their  $\Phi(\mathbf{r})$ , is now possible in  $\text{Bi}_2\text{Sr}_2\text{CaCu}_2\text{O}_{8+x}$ .

The pivotal question is then: how does displacement of the apical oxygen atom  $\delta(\mathbf{r})$  alter the charge transfer energy  $\mathcal{E}(\mathbf{r})$  and the electron-pair density  $n_p(\mathbf{r})$  at each Cu atom<sup>7,8,9,39,40,41,42</sup>, within the  $\text{Bi}_2\text{Sr}_2\text{CaCu}_2\text{O}_{8+x}$  supermodulation (Fig. 5a)? To synthesize data as in Fig. 4, we first plot apical distance alterations versus phase  $\delta(\Phi)$  for  $\text{Bi}_2\text{Sr}_2\text{CaCu}_2\text{O}_{8+x}$ , as shown by grey dots in Fig. 5b. We then process  $\mathcal{E}(\mathbf{r})$  retaining only wavevectors close to  $\pm \mathbf{Q}_S$ . Then, by corresponding simultaneous  $\Phi(\mathbf{r}) : \mathcal{E}(\mathbf{r})$  measurements (e.g. Fig. 4a,c) we

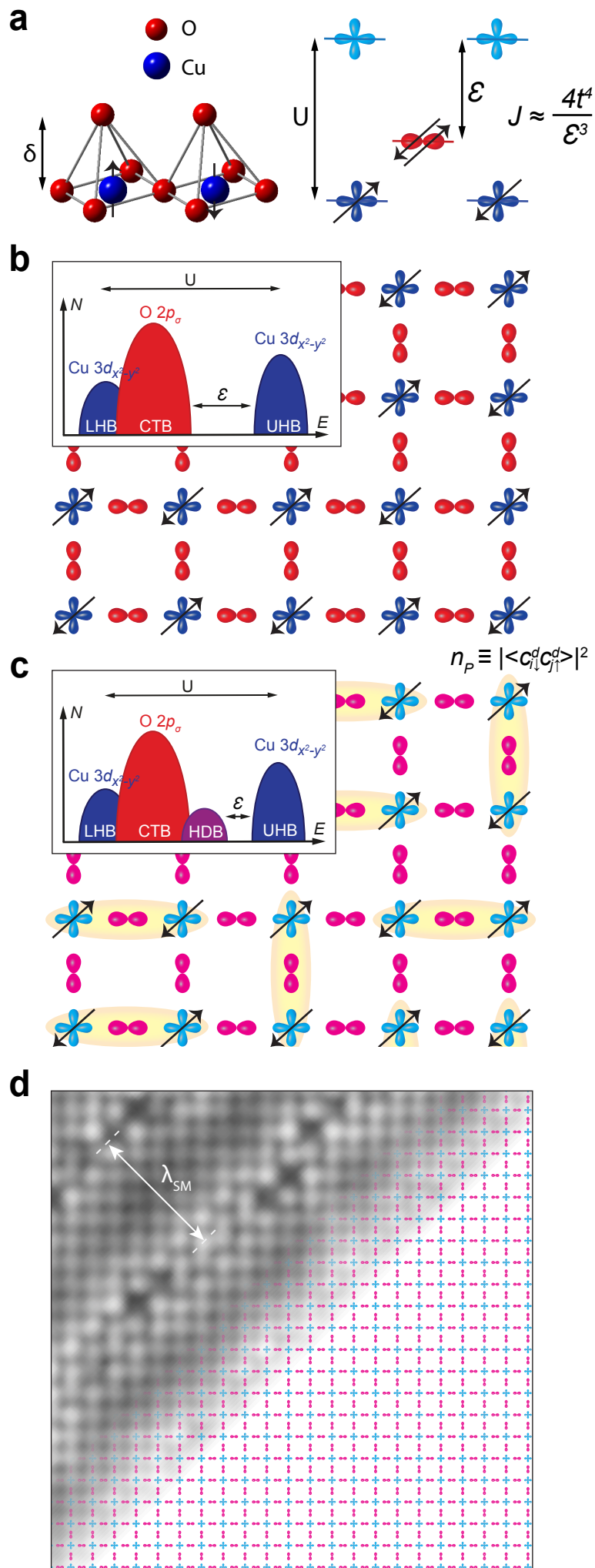
determine  $\mathcal{E}(\Phi)$  shown as red dots in Fig. 5b; this is found to be a very repeatable characteristic of  $\text{Bi}_2\text{Sr}_2\text{CaCu}_2\text{O}_{8+x}$  (see SI Figs 4 and 5). Similarly, by corresponding simultaneous  $\Phi(\mathbf{r}) : n_p(\mathbf{r})$  measurements (e.g. Fig. 4b,d) we determine  $\bar{n}_p(\Phi)$  which is normalized to the mean value of measured  $n_p(\mathbf{r})$ . This is shown by blue dots in Fig. 5b; this is another repeatable characteristic (SI Section ‘Determination of Relationships  $\mathcal{E}(\Phi)$  and  $n_p(\Phi)$ ’). The microscopic relationship of  $\mathcal{E}$  to  $\delta$  can then be determined by eliminating common variable  $\Phi$  from Fig. 5b. The result, shown in Fig. 5c, provides a direct measurement of this long-sought characteristic<sup>7,8,9,39,40,41</sup> of cuprate electronic structure:  $d\mathcal{E}/d\delta \approx -1.04 \pm 0.12 \text{ eV/\AA}$  and  $d\bar{n}_p/d\delta \approx 0.85 \pm 0.22 \text{ \AA}^{-1}$  for  $\text{Bi}_2\text{Sr}_2\text{CaCu}_2\text{O}_{8+x}$ . Ultimately, the atomic-scale relationship between the normalized electron-pair density  $\bar{n}_p$  and the charge-transfer energy  $\mathcal{E}$  is derived by eliminating the common variable  $\delta$  from Fig. 5c. The result as shown in Fig. 5D, demonstrates that  $d\bar{n}_p/d\mathcal{E} \approx -0.81 \pm 0.17 \text{ eV}^{-1}$  or equivalently that  $d|\overline{c_\uparrow c_\downarrow}|/d\mathcal{E} \approx 0.40 \pm 0.09 \text{ eV}^{-1}$  for  $\text{Bi}_2\text{Sr}_2\text{CaCu}_2\text{O}_{8+x}$ .

Although the original predictions<sup>7,8</sup> for  $d\mathcal{E}/d\delta$  were for  $\text{La}_2\text{CuO}_4$ , they are still in remarkably good agreement with our observations for  $\text{Bi}_2\text{Sr}_2\text{CaCu}_2\text{O}_{8+x}$  as shown in Fig. 5d. Predictions for the direct effect on the cuprate electron-pair wavefunction of altering the charge-transfer  $\mathcal{E}$  yield (SI Section ‘Estimation of  $\alpha$  from three-band  $\text{CuO}_2$  Hubbard model calculations’)  $d|\overline{c_\uparrow c_\downarrow}|/d\mathcal{E} \approx -\alpha/2 \text{ eV}^{-1}$  or equivalently  $d\bar{n}_p/d\mathcal{E} \approx -\alpha \text{ eV}^{-1}$ , with a range  $0.3 \lesssim \alpha \lesssim 1.0$  depending on the material-specific parameters<sup>7,8,9,10</sup>. Figure 5e indicates the anticipated range of  $\alpha$  for different materials using a yellow shaded triangle. For  $\text{Bi}_2\text{Sr}_2\text{CaCu}_2\text{O}_8$  specifically<sup>10</sup>, the three-band  $\text{CuO}_2$  Hubbard model predictions for a superexchange electron-pairing mechanism is that  $d|\overline{c_\uparrow c_\downarrow}|/d\mathcal{E} \approx 0.46 \pm 0.05 \text{ eV}^{-1}$  or equivalently that  $\alpha \approx 0.93 \pm 0.1 \text{ eV}^{-1}$ . The agreement with experimental observations reported in Fig. 5e is self-evident.

To recapitulate: by visualizing the electron-pair density  $n_p(\mathbf{r})$  using SJTM (e.g., Fig. 4d,f), and the charge transfer energy  $\mathcal{E}(\mathbf{r})$  using high-voltage SISTM (e.g., Fig. 4c,e), we find empirically that both modulate strongly at the  $\text{Bi}_2\text{Sr}_2\text{CaCu}_2\text{O}_{8+x}$  crystal supermodulation wavevector  $\mathbf{Q}_s$  (Fig. 2b,c; Fig. 5b). Then, by mapping the displacement  $\delta$  of apical O from

planar Cu atoms (Fig. 3d) due to this supermodulation, we demonstrate that theoretical predictions for  $\mathcal{E}(\delta)$  and  $n_p(\delta)$  conform well to the measured characteristics of both  $d\mathcal{E}/d\delta$  and  $d\bar{n}_p/d\delta$  (Fig. 5c,d). Our demonstration that  $d|\langle c_{\uparrow}c_{\downarrow} \rangle|/d\mathcal{E} < 0$  (Fig. 5e) has long been anticipated by pioneering theories of superexchange mediated electron pairing in cuprates<sup>20,21,22,23,24,25,26,27,28,29</sup>. More specifically, the recent numerical studies of the three-band CuO<sub>2</sub> Hubbard model<sup>7,8,9,10</sup>, within which charge-transfer superexchange is demonstrably the cause of electron pairing<sup>11,30-36</sup>, yield quantitative agreement between predicted  $d|\overline{\langle c_{\uparrow}c_{\downarrow} \rangle}|/d\mathcal{E} \approx -0.46 \pm 0.05 \text{ eV}^{-1}$  and our experimental determination that  $d\bar{n}_p/d\mathcal{E} \approx -0.81 \pm 0.17 \text{ eV}^{-1}$  for Bi<sub>2</sub>Sr<sub>2</sub>CaCu<sub>2</sub>O<sub>8+x</sub>. Because exact predictions of atomic-scale crystal geometry effects on  $\mathcal{E}$  or  $\langle c_{\uparrow}c_{\downarrow} \rangle$  or  $n_p$  are quite complex<sup>42</sup>, cluster DMFT analysis of  $N(E)$ ,  $\mathcal{E}$  and  $\langle c_{\uparrow}c_{\downarrow} \rangle$  throughout a complete Bi<sub>2</sub>Sr<sub>2</sub>CaCu<sub>2</sub>O<sub>8+x</sub> supermodulation period would now be highly advantageous. Nevertheless, taken at face value the data in Fig. 5 establish that charge-transfer superexchange is key to the electron-pairing mechanism of the hole-doped cuprate superconductor Bi<sub>2</sub>Sr<sub>2</sub>CaCu<sub>2</sub>O<sub>8+x</sub>.

FIG 1



## FIGURES

**Figure 1: Superexchange Magnetic Interactions in Transition-metal Oxides**

- a. Schematic representation of  $\text{CuO}_5$  pyramids whose bases comprise the  $\text{CuO}_2$  plane. The degeneracy of Cu  $d_{x^2-y^2}$  orbitals (blue) is lifted by U, and the O  $p_\sigma$  orbitals (red) are separated from the upper Cu  $d_{x^2-y^2}$  band by the charge transfer energy  $\mathcal{E}$  (for holes).
- b. Schematic of antiferromagnetic charge-transfer insulator state in undoped  $\text{CuO}_2$ . Inset shows a schematic density of electronic states  $N(E)$  in this phase, with the Coulomb energy U and the charge transfer energy  $\mathcal{E}$  indicated.
- c. Schematic of hole-doped  $\text{CuO}_2$ , a two-dimensional correlated metallic state with intense antiferromagnetic spin-spin interactions. When superconductive, the electron-pair wavefunction  $\Psi \equiv \langle c_{i\downarrow}^d c_{j\uparrow}^d \rangle$  is indicated schematically in yellow, and the related electron-pair density is  $n_p \equiv |\langle c_{i\downarrow}^d c_{j\uparrow}^d \rangle|^2$ . Inset shows a schematic  $N(E)$  in this phase which, although reorganized by the delocalized carriers, still retains a charge-transfer energy scale  $\mathcal{E}$ .
- d. Schematic of  $\text{CuO}_2$  partially overlaid by a  $\text{Bi}_2\text{Sr}_2\text{CaCu}_2\text{O}_{8+x}$  topographic image  $T(\mathbf{r})$  to exemplify how the crystal supermodulation modulates along the (1,1) axis, with one period  $0 \leq \Phi \leq 2\pi$  requiring approximately  $26 \text{ \AA}$ . The Cu to apical O distance  $\delta$  is modulated at same wavevector but perpendicular to this plane.

FIG 2

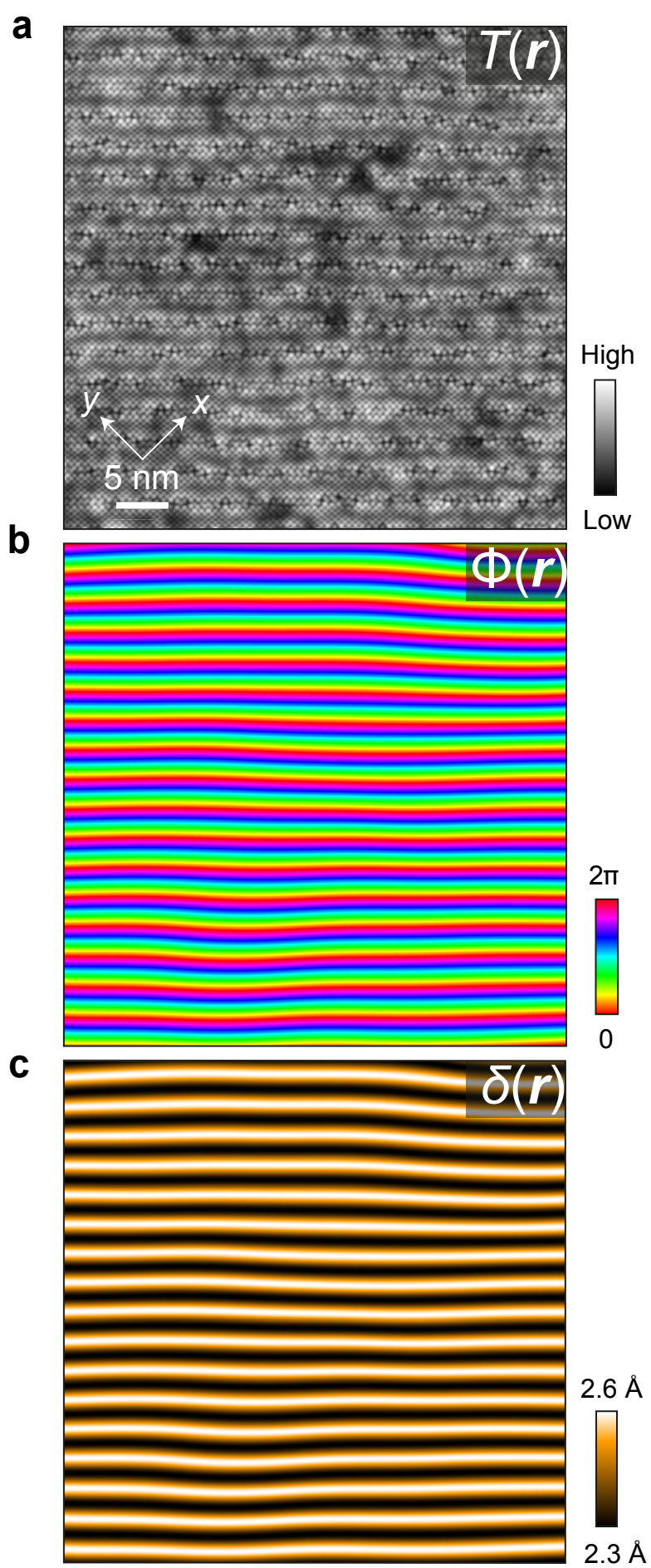




**Figure 2: Imaging the Apical Oxygen to Planar Copper Distance  $\delta(\mathbf{r})$**

- a. Exemplary  $\text{Bi}_2\text{Sr}_2\text{CaCu}_2\text{O}_{8+x}$  topograph  $T(\mathbf{r})$  at the BiO termination layer. The planar Cu-O axes are at 45-degrees to the supermodulation, as shown. The supermodulation runs from top to bottom with wavevector  $\mathbf{Q}_S \approx (0.15, 0.15)2\pi/a_0$ , obviously with relatively short correlation length.
- b. From a, the supermodulation phase  $\Phi(\mathbf{r})$  is derived (SI Section ‘Supermodulation phase  $\Phi(\mathbf{r})$  and apical displacement  $\delta(\mathbf{r})$ ’).
- c. From b, the apical distance  $\delta(\mathbf{r})$  is derived from X-ray refinement data for the  $\text{Bi}_2\text{Sr}_2\text{CaCu}_2\text{O}_{8+x}$  crystal structure (SI Section ‘Supermodulation phase  $\Phi(\mathbf{r})$  and apical displacement  $\delta(\mathbf{r})$ ’).

FIG 3

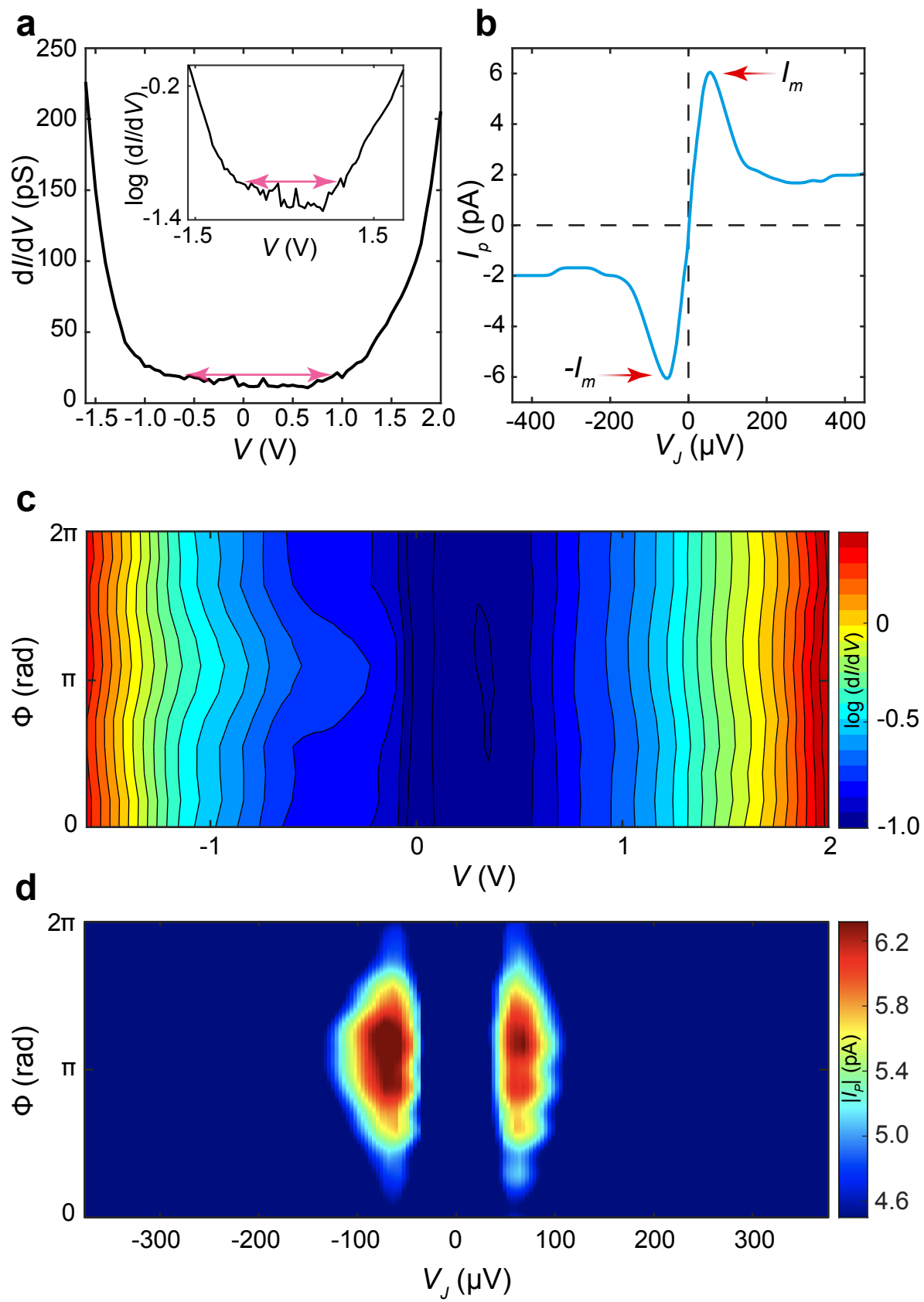


**Figure 3: Visualizing Charge-Transfer Energy  $\mathcal{E}$  and Electron-Pair Density  $n_p$**

- a. Typical  $g(V)$  spectrum of single-electron tunneling measured at high-voltage and high tunnel junction resistance  $R_N \approx 85 \text{ G}\Omega$ . Inset:  $\log(g(V))$  indicates exponential growth of density of states away from gap edges<sup>44</sup>. The estimated value of  $\mathcal{E}$  is derived as the minimum energy separation between the bands at constant  $g = 20 \text{ pS}$ , as shown by double-head pink arrows. Any other choice of  $g > 20 \text{ pS}$  at which  $\mathcal{E}$  is estimated yields qualitatively similar results (SI Section ‘Charge transfer energy visualization  $\mathcal{E}(r)$  by SISTM’).
- b. Typical  $I_p(V_J)$  spectrum of electron-pair tunneling measured at low-voltage, low  $R_N$ . The maximum and minimum current values  $\pm I_m$  are indicated with red arrows.
- c. Contour plot of measured  $g(\Phi, V)$  versus bias voltage  $V$  and supermodulation phase  $\Phi$ . The modulation of the charge-transfer energy  $\mathcal{E}$  is clear (SI Section ‘Charge transfer energy visualization  $\mathcal{E}(r)$  by SISTM’).
- d. Contour plot of a typical measured  $|I_p(\Phi, V_J)|$  versus Josephson-junction bias voltage  $V_J$  and supermodulation phase  $\Phi$ , in which the modulation of maximum electron-pair tunneling rate is obvious (SI Section ‘Electron-pair density visualization  $n_p(r)$  by SJTM’).

FIG 4

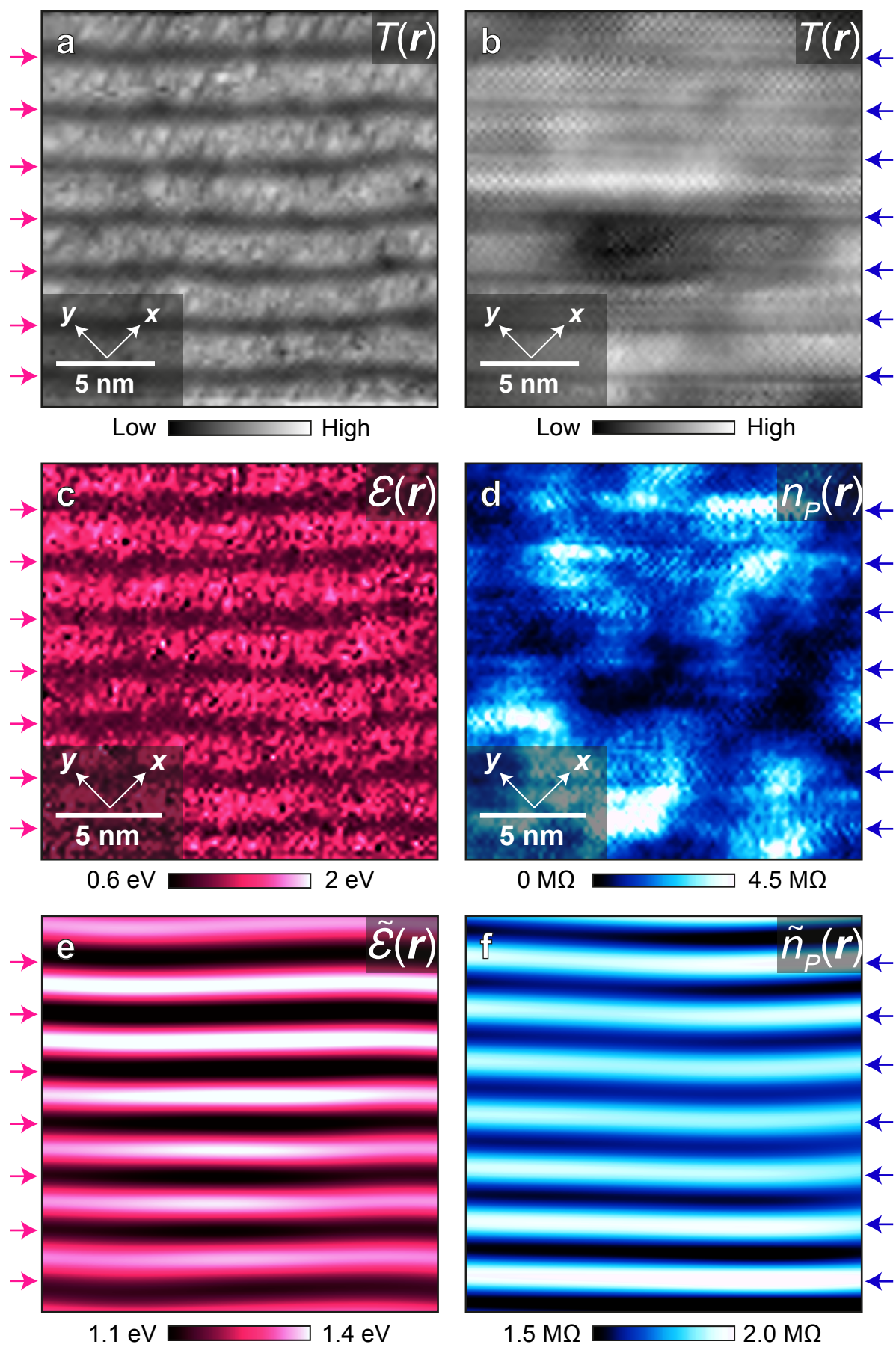


**Figure 4: Atomic-scale Visualization of  $\mathcal{E}(\mathbf{r})$  and  $n_p(\mathbf{r})$  Versus  $\delta(\mathbf{r})$**

- a. Topographic image  $T(\mathbf{r})$  simultaneous with high-voltage  $g(\mathbf{r}, V)$  measured at  $R_N \approx 85 \text{ G}\Omega$  yielding c. The pink arrowheads are at  $\Phi = \pi$  as determined using the procedures described in SI Section ‘Supermodulation phase  $\Phi(\mathbf{r})$  and apical displacement  $\delta(\mathbf{r})$ ’.
- b. Topographic image  $T(\mathbf{r})$  simultaneous with low-voltage  $I_p(\mathbf{r}, V_J)$  and  $R_N(\mathbf{r})$  maps yielding d. The blue arrowheads are at  $\Phi = \pi$  as determined using the procedures described in SI Section ‘Supermodulation phase  $\Phi(\mathbf{r})$  and apical displacement  $\delta(\mathbf{r})$ ’. The topographic image has atomic resolution allowing the BiO layer to be discerned clearly, although it is somewhat different than a, due to use of a  $\text{Bi}_2\text{Sr}_2\text{CaCu}_2\text{O}_{8+x}$  nanoflake superconductive tip<sup>17</sup> (SI Section ‘Electron-pair density visualization  $n_p(\mathbf{r})$  by SJTM’).
- c. Measured  $\mathcal{E}(\mathbf{r})$  in the FOV of a. The mean value is  $\mathcal{E} = 1.195 \text{ eV}$ , which is in very good agreement with  $\mathcal{E}(\mathbf{r})$  for  $\text{Bi}_2\text{Sr}_2\text{CaCu}_2\text{O}_{8+x}$  derived independently from other techniques (SI Section ‘Charge transfer energy visualization  $\mathcal{E}(\mathbf{r})$  by SISTM). The pink arrowheads are at  $\Phi = \pi$  of the supermodulation.
- d. Measured  $n_p(\mathbf{r})$  in the FOV of b. (SI Section ‘Electron-pair density visualization  $n_p(\mathbf{r})$  by SJTM’). The blue arrowheads are at  $\Phi = \pi$ .
- e. Fourier filtered  $\mathcal{E}(\mathbf{r})$  at supermodulation wavevectors  $\pm \mathbf{Q}_S$  in the FOV of a,c. The pink arrowheads are at  $\Phi = \pi$ .
- f. Fourier filtered  $n_p(\mathbf{r})$  at supermodulation wavevectors  $\pm \mathbf{Q}_S$  in the FOV of b,d. The blue arrowheads are at  $\Phi = \pi$ .

FIG 5

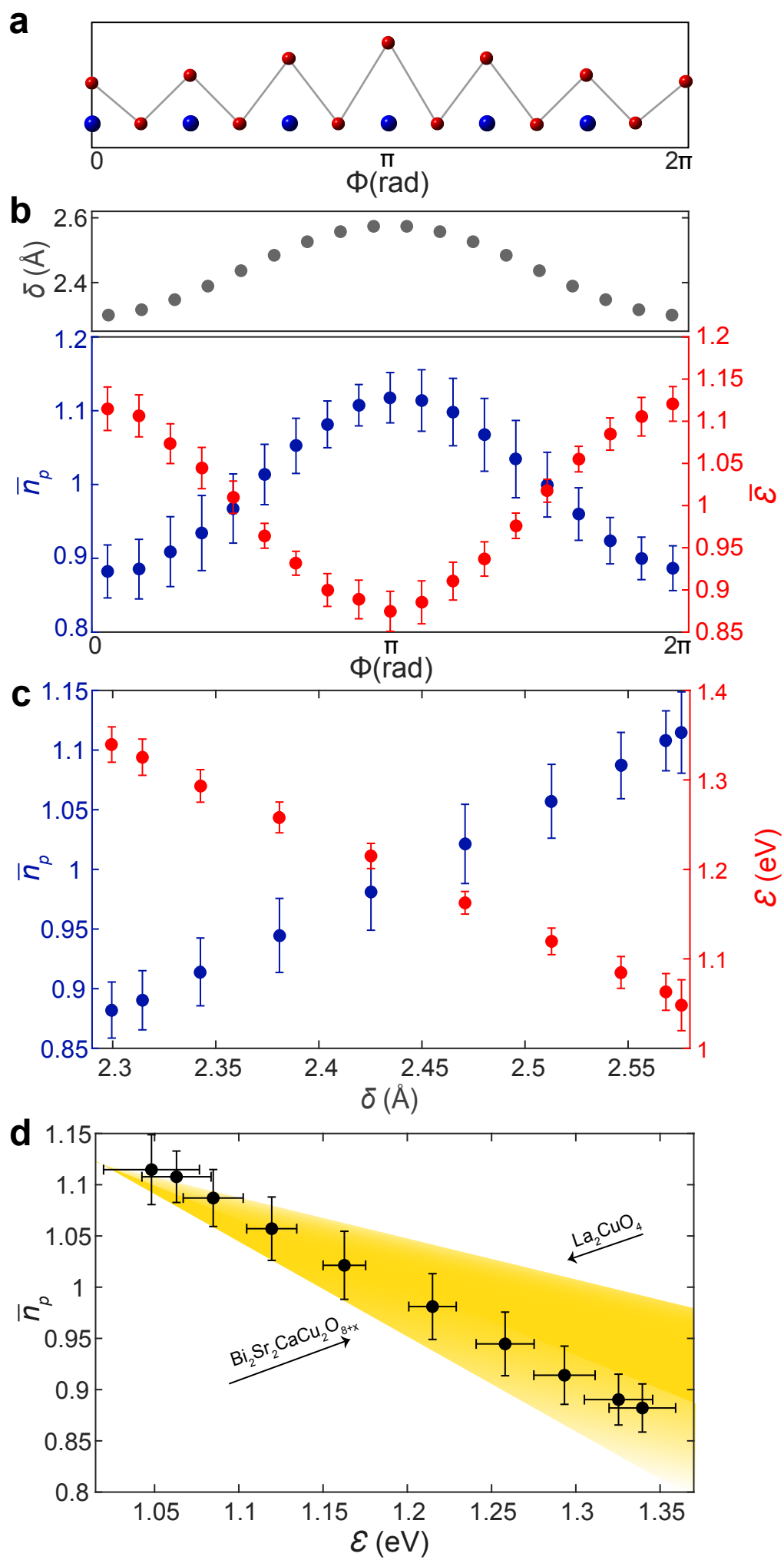


**Figure 5: Evolution of Cuprate Electron-pair Density  $n_p$  with Charge-Transfer Gap  $\mathcal{E}$**

- a. Schematic of planar Cu to apical O distance modulations  $\delta(\mathbf{r})$  in  $\text{Bi}_2\text{Sr}_2\text{CaCu}_2\text{O}_{8+x}$  shown versus supermodulation phase  $\Phi$ .
- b. Grey dots:  $\delta(\Phi)$  showing the displacement of the apical oxygen atom within the  $\text{CuO}_5$  pyramid versus supermodulation phase  $\Phi$ .  
Red dots: measured  $\mathcal{E}(\Phi)$  showing the typical value for the Cu-O charge-transfer energy  $\mathcal{E}$  for each value of the supermodulation phase  $\Phi$ . These data are from the same FOV as 4 a,c,e. Blue dots: measured  $n_p(\Phi)$  showing the measured value of electron-pair density versus supermodulation phase  $\Phi$ . These data are from a larger FOV which contains the FOV from 4 b,d,f.
- c. Measured dependence of Cu-O charge-transfer energy  $\mathcal{E}$  and electron-pair density  $n_p$  on the displacement  $\delta$  of the apical O atoms from the planar Cu atoms.
- d. Measured relationship of electron-pair density  $n_p$  to the Cu-O charge-transfer energy  $\mathcal{E}$  in the  $\text{CuO}_2$  plane of  $\text{Bi}_2\text{Sr}_2\text{CaCu}_2\text{O}_{8+x}$ . The yellow shaded region shows the range of predicted slopes for  $d\bar{n}_p/d\mathcal{E} \equiv -\alpha$ , as  $0.3 \lesssim \alpha \lesssim 1.0 \text{ eV}^{-1}$ . These are derived from DMFT calculations for various materials with the limits reported for  $\text{La}_2\text{CuO}_4$  and  $\text{Bi}_2\text{Sr}_2\text{CaCu}_2\text{O}_{8+x}$  as indicated by black arrows.

**Acknowledgements:** We acknowledge and thank S.D. Edkins, K. Fujita and J. Zaanen for helpful discussions and advice. We are grateful to D.-H. Lee for critical theoretical guidance on the interplay of superexchange with the electron-pair wavefunctions. M.H.H, X.L., Y.X.C., and J.C.S.D acknowledge support from the Moore Foundation's EPiQS Initiative through Grant GBMF9457. S.O'M and J.C.S.D. acknowledge support from Science Foundation of Ireland under Award SFI 17/RP/5445. W.C. and J.C.S.D. acknowledge support from the Royal Society under Award R64897. W.R. and J.C.S.D. acknowledge support from the European Research Council (ERC) under Award DLV-788932.

**Author Contributions:** J.C.S.D. conceived and supervised the project. H.E. and S.U. synthesized and characterized the samples; M.H.H. carried out SJTM measurements and data processing; S.O'M, W.R., Y.X.C., X.L. and W.C. developed and carried out the comprehensive analysis. J.C.S.D. wrote the paper with key contributions from S.O'M, W.R. and W.C. The manuscript reflects the contributions and ideas of all authors.

**Author Information** Reprints and permissions information is available at [www.nature.com/reprints](http://www.nature.com/reprints). The authors declare no competing financial interests. Readers are welcome to comment on the online version of the paper. Correspondence and requests for materials should be addressed to [jcseamusdavis@gmail.com](mailto:jcseamusdavis@gmail.com).



## References

---

- 1 Keimer, B., Kivelson, S. A., Norman, M. R., Uchida, S. & Zaanen, J. From quantum matter to high-temperature superconductivity in copper oxides. *Nature* **518**, 179-186 (2015)
- 2 Zaanen, J., Sawatzky, G. A. & Allen, J. W. Band gaps and electronic structure of transition-metal compounds. *Phys. Rev. Lett.* **55**, 418 (1985)
- 3 Anderson, P.W. New Approach to the Theory of Superexchange Interactions. *Phys. Rev.* **115**, 2 (1959)
- 4 Eskes, H. & Jefferson, J.H. Superexchange in the cuprates. *Phys. Rev. B* **48**, 9788 (1993)
- 5 Anderson, P.W. The Resonating Valence Bond State in  $\text{La}_2\text{CuO}_4$  and Superconductivity. *Science* **235**, 1196-1198 (1987)
- 6 Weber, C., Haule, K. & Kotliar, G. Strength of correlations in electron- and hole-doped cuprates. *Nat. Phys.* **6**, 574-578 (2010)
- 7 Weber, C., Yee, C., Haule, K. & Kotliar, G. Scaling of the transition temperature of hole-doped cuprate superconductors with the charge-transfer energy. *Europhys. Lett.* **100**, 37001 (2012)
- 8 Yee, C.-H. & Kotliar, G. Tuning the charge-transfer energy in hole-doped cuprates. *Phys. Rev. B* **89**, 094517 (2014)
- 9 Acharya, S. et al. Metal-Insulator Transition in Copper Oxides Induced by Apex Displacements. *Phys. Rev. X* **8**, 021038 (2018)
- 10 Kowalski N., Dash S., S  n  chal D., Tremblay A. -M. S. Oxygen hole content, charge-transfer gap, covalency, and cuprate superconductivity [arXiv:2104.07087](https://arxiv.org/abs/2104.07087) (2021)
- 11 Mai P., Balduzzi G., Johnston S., Maier T.A., Pairing correlations in the cuprates: a numerical study of the three-band Hubbard model, *Phys. Rev. B* **103**, 144514 (2021)
- 12 R. Coldea, S. M. Hayden, G. Aeppli, T. G. Perring, C. D. Frost, T. E. Mason, S.-W. Cheong, and Z. Fisk, Spin Waves and Electronic Interactions in  $\text{La}_2\text{CuO}_4$ , *Phys. Rev. Lett.* **86**, 5377 (2001)
- 13 Arovas, D.P., Berg, E., Kivelson S.A., Raghu S., The Hubbard Model [arxiv:2103.12097](https://arxiv.org/abs/2103.12097) (2021)
- 14 Qin Mingpu, Sch  fer T., Andergassen S., Corboz P., Gull E. The Hubbard model: A computational perspective [arXiv:2104.00064](https://arxiv.org/abs/2104.00064) (2021)
- 15   makov J., Martin I., and Balatsky A.V., Josephson scanning tunneling microscopy *Phys. Rev. B* **64**, 212506 (2001)

- 
- 16 Graham M., Dirk K. Morr, Josephson Scanning Tunneling Spectroscopy in dx<sup>2</sup>-y<sup>2</sup>-wave superconductors: a probe for the nature of the pseudo-gap in the cuprate superconductors Phys. Rev. Lett. **123**, 017001 (2019)
  - 17 Hamidian, M.H. et al. Detection of a Cooper-pair density wave in Bi<sub>2</sub>Sr<sub>2</sub>CaCu<sub>2</sub>O<sub>8+x</sub>. Nature **532**, 343-347 (2016).
  - 18 Cho, D., Bastiaans, K.M., Chatzopoulos, D., Gu, G.D. & Allan, M.P. A strongly inhomogeneous superfluid in an iron-based superconductor. Nature **571**, 541-545 (2019).
  - 19 Liu, X., Chong, Y.-X., Sharma, R. & Davis, J.C. Discovery of a Cooper-Pair Density Wave State in a Transition-Metal Dichalcogenide. Science **372** 1447 (2021)
  - 20 Emery, V.J. Theory of high-T<sub>c</sub> superconductivity in oxides. Phys. Rev. Lett **58**, 2794 (1987).
  - 21 Zhang, F.C. & Rice, T.M. Effective Hamiltonian for the superconducting Cu oxides. Phys. Rev. B **37**, 3759(R) (1988)
  - 22 Zhang, F.C., Gros, C., Rice, T.M., and Shiba, H. A renormalised Hamiltonian approach to a resonant valence bond wavefunction. Supercond. Sci. Technol. **1**, 36 (1988)
  - 23 Ruckenstein A.E., Hirschfeld P.J., and Appel J., Mean-field theory of high-T<sub>c</sub> superconductivity: The superexchange mechanism Phys. Rev. B **36**, 857(R) (1987)
  - 24 Kotliar, G. and Liu, J. Superexchange mechanism and d-wave superconductivity. Phys. Rev. B **38**, 5142(R) (1988)
  - 25 Lee, P.A. et al. SU(2) formulation of the  $t - J$  model: Application to underdoped cuprates. Phys. Rev. B **57**, 6003 (1998)
  - 26 Scalettar, R.T., Scalapino, D.J., Sugar, R.L. & White, S.R. Antiferromagnetic, charge-transfer, and pairing correlations in the three-band Hubbard model. Phys. Rev. B **44**, 770 (1991)
  - 27 Paramekanti, A., Randeria, M. & Trivedi, N. Projected Wave Functions and High Temperature Superconductivity Phys. Rev. Lett. **87**, 217002 (2001)
  - 28 Anderson, P.W. et al. The physics behind high-temperature superconducting cuprates: the 'plain vanilla' version of RVB. J. Phys.: Condens. Matter **16**, R755 (2004)
  - 29 Lee, P.A., Nagaosa, N. & Wen, X.-G. Doping a Mott insulator: Physics of high-temperature superconductivity. Rev. Mod. Phys. **78**, 17 (2006)
  - 30 Poilblanc, D. & Scalapino, D. J. Calculation of  $\Delta(k, \omega)$  for a two-dimensional  $t - J$  cluster. Phys. Rev. B **66**, 052513 (2002)

- 
- 31 Haule, K. & Kotliar, G. Strongly correlated superconductivity: A plaquette dynamical mean-field theory study. *Phys. Rev. B* **76**, 104509 (2007)
  - 32 Maier, T. A., Poilblanc, D., and Scalapino, D. J. Dynamics of the Pairing Interaction in the Hubbard and  $t - J$  Models of High-Temperature Superconductors. *Phys Rev. Lett.* **100**, 237001 (2008)
  - 33 Kancharla, S. S. et al. Anomalous superconductivity and its competition with antiferromagnetism in doped Mott insulators. *Phys. Rev. B* **77**, 184516 (2008)
  - 34 Gull, E. and Millis, A.J. Pairing glue in the two-dimensional Hubbard model. *Phys. Rev. B* **90**, 041110(R) (2014)
  - 35 Romer, A. et al. Pairing in the two-dimensional Hubbard model from weak to strong coupling. *Phys. Rev. Res.* **2**, 013108 (2020)
  - 36 Mai, Peizhi, Balduzzi G., Johnston S., Maier T.A., Pairing correlations in the cuprates: a numerical study of the three-band Hubbard model *Phys. Rev. B* **103**, 144514 (2021)
  - 37 Reynolds, C. A., Serin, B., Wright, W. H., & Nesbitt, L. B. Superconductivity of Isotopes of Mercury. *Physical Review* **78**, 487 (1950)
  - 38 Emery, V. J. & Kivelson, S. A. Importance of phase fluctuations in superconductors with small superfluid density. *Nature* **374**, 434–437 (1995)
  - 39 Ohta, Y., Tohyama, T. & Maekawa, S. Electronic structure of insulating cuprates: Role of Madelung potential in the charge-transfer gap and superexchange interaction. *Physica C* **185-189**, 1721-1722 (1991)
  - 40 Feiner, L., Grilli, M. & Di Castro, C. Apical oxygen ions and the electronic structure of the high- $T_c$  cuprates. *Phys. Rev. B* **45**, 10647 (1992)
  - 41 Pavarini, E., Dasgupta, I., Saha-Dasgupta, T., Jepsen, O. & Anderson, O.K. Band-Structure Trend in Hole-Doped Cuprates and Correlation with  $T_c$  max. *Phys Rev. Lett.* **87**, 047003 (2001)
  - 42 Foyevtsova, K., Valenti, R. & Hirschfeld, P.J. Effect of dopant atoms on local superexchange in cuprate superconductors: A perturbative treatment. *Phys. Rev. B* **79**, 144424 (2009)
  - 43 Gao, Y *et al*, The Incommensurate Modulation of the 2212 Bi-Sr-Ca-Cu-O Superconductor *Science* **241**, 954 (1988).

- 
- 44 Cai, P. et al. Visualizing the evolution from the Mott insulator to a charge-ordered insulator in lightly doped cuprates. *Nat. Phys.* **12**, 1047–1051 (2016)

Supplementary Information for

**On the Electron Pairing Mechanism of  
Copper-Oxide High Temperature Superconductivity**

S.M. O'Mahony, Wangping Ren, Weijiong Chen, Yi Xue Chong, Xiaolong Liu,  
H. Eisaki, S. Uchida, M.H. Hamidian, and J.C. Séamus Davis

**(I) Measuring Charge Transfer Energy, Superexchange and Superconductivity**

Many types of studies of  $\mathcal{E}$  and its consequent  $J$  for cuprates have been carried out on bulk crystals. Optical reflectivity<sup>1,2</sup> revealed that the charge transfer energy in the parent insulating state (Fig. 1b), for virtually all cuprates that become superconducting under hole-doping, is  $1 \text{ eV} < \mathcal{E} < 2 \text{ eV}$ . Raman<sup>1,2,3</sup> identified the concomitant electron-pair excitations as a superexchange energy in the range  $J \sim 150 \text{ meV}$ . Single electron spectroscopy by tunneling<sup>4</sup> reveals that the charge transfer energy for  $\text{Bi}_2\text{Sr}_2\text{CaCu}_2\text{O}_{8+x}$  in the insulating parent state is  $\mathcal{E} \gtrsim 1 \text{ eV}$ , and a non-monotonic but diminishing trend of maximum  $T_c$  measured in the superconductor with increasing  $\mathcal{E}$  measured in the corresponding insulator, for samples of several distinct material types. Advanced angle resolved photoemission<sup>5</sup> reports transitions to unoccupied states consistent with a Cu on-site Coulomb interaction strength  $U$  of  $2.7 \text{ eV}$  and that the charge-transfer energy of optimally doped  $\text{Bi}_2\text{Sr}_2\text{CaCu}_2\text{O}_{8+x}$  is  $\mathcal{E} \approx 1.1 \text{ eV}$ . Most recently, resonant inelastic X-ray scattering<sup>6</sup> reveals directly, from the spectrum of spin wave excitations of many cuprate materials, that  $140 \text{ meV} < J < 180 \text{ meV}$ .

**(II) Supermodulation Phase  $\Phi(\mathbf{r})$  and Apical Displacement  $\delta(\mathbf{r})$**

The crystal supermodulation in  $\text{Bi}_2\text{Sr}_2\text{CaCu}_2\text{O}_{8+x}$  perturbs the atoms from their idealized crystal positions due to the mismatch between the bond lengths of the rock-salt layer and the perovskite layer of  $\text{Bi}_2\text{Sr}_2\text{CaCu}_2\text{O}_{8+x}$ . The modulation has a periodicity of  $\sim 26 \text{ \AA}$  along the  $a$ -axis of the crystal<sup>7</sup>. The distance between all atoms in each  $\text{Bi}_2\text{Sr}_2\text{CaCu}_2\text{O}_{8+x}$  unit cell modulates periodically, with the change in distance between the planar Cu atom and the apical O atom being largest in amplitude (SI Fig. 1) varying between  $2.25 \text{ \AA}$  and  $2.54 \text{ \AA}$  over one supermodulation period (Fig 5a). X-ray scattering data<sup>7</sup> also reveals that the Bi-O distance is virtually constant over the supermodulation

period (SI Fig. 1), enabling direct connection between the supermodulation signal in the topographic image  $T(\mathbf{r})$  and the modulation of the planar Cu to apical O separation  $\delta(\mathbf{r})$  (SI Fig. 1). SI Fig. 1 also shows the displacement of the BiO termination layer from the symmetry plane of the crystal, which is equivalent to a topograph  $T(\mathbf{r})$ . This allows one to directly relate the supermodulation phase  $\Phi$  obtained from  $T(\mathbf{r})$  to the X-ray refinement data<sup>7</sup>.

Effects of the supermodulation can be observed in topographic images  $T(\mathbf{r})$  measured at the BiO crystal termination layer of  $\text{Bi}_2\text{Sr}_2\text{CaCu}_2\text{O}_{8+x}$ . Its signal as a component of the topographic image can be expressed as

$$T'(\mathbf{r}) = A_s(\mathbf{r}) \cos \Phi(\mathbf{r}), \quad (1)$$

$$\Phi(\mathbf{r}) = \mathbf{Q}_s \cdot \mathbf{r} + \theta(\mathbf{r}), \quad (2)$$

where  $\mathbf{Q}_s$  is the supermodulation vector and  $\theta(\mathbf{r})$  is a spatially dependent phase disorder. To measure  $\Phi(\mathbf{r})$  we process  $T(\mathbf{r})$  retaining only the wavevector components near  $\mathbf{q} = \pm \mathbf{Q}_s$ . In practice, this is achieved by first Fourier filtering  $T(\mathbf{r})$  as follows:

$$T'(\mathbf{r}) = \frac{1}{\sigma\sqrt{2\pi}} \int T(\mathbf{q}) \left( e^{\frac{|\mathbf{q}-\mathbf{Q}_s|^2}{2\sigma^2}} + e^{\frac{|\mathbf{q}+\mathbf{Q}_s|^2}{2\sigma^2}} \right) \exp(-i\mathbf{q} \cdot \mathbf{r}) d\mathbf{q} \quad (3)$$

where  $T(\mathbf{q})$  is the Fourier transform of  $T(\mathbf{r})$ . We use  $\sigma \approx \frac{2\pi}{20} \text{ nm}^{-1}$  when filtering  $\mathcal{E}(\mathbf{r})$  and  $\sigma \approx \frac{2\pi}{40} \text{ nm}^{-1}$  when filtering  $n_p(\mathbf{r})$ , to take account of the difference in tip sizes. Next, to visualize the phase disorder  $\theta(\mathbf{r})$ , we employ a two-dimensional lock-in method in which references  $\alpha(\mathbf{r}) = \sin(\mathbf{Q}_s \cdot \mathbf{r})$  and  $\beta(\mathbf{r}) = \cos(\mathbf{Q}_s \cdot \mathbf{r})$  are multiplied by  $T'(\mathbf{r})$ :

$$X(\mathbf{r}) \equiv T'(\mathbf{r})\alpha(\mathbf{r}), \quad (4)$$

$$Y(\mathbf{r}) \equiv T'(\mathbf{r})\beta(\mathbf{r}). \quad (5)$$

Low pass filtering these product images to remove the AC term, yields

$$\theta(\mathbf{r}) = \arctan\left(\frac{Y(\mathbf{r})}{X(\mathbf{r})}\right). \quad (6)$$

Adding back the pure modulating  $\mathbf{Q}_s \cdot \mathbf{r}$  term and defining the result modulo  $2\pi$ , generates a map of the total supermodulation phase  $\Phi(\mathbf{r}) = [\mathbf{Q}_s \cdot \mathbf{r} + \theta(\mathbf{r})] \bmod 2\pi$ .

The relationship between the apical Cu-O displacement  $\delta$  and the supermodulation phase  $\Phi$  can then be obtained using X-ray refinement techniques<sup>7</sup> that report apical displacement varies between  $\delta \sim 2.25 \text{ \AA}$  at  $\Phi = 0$  and  $\delta \sim 2.54 \text{ \AA}$  at  $\Phi = \pi$  (SI Fig. 1) The first harmonic is reported as:

$$\delta(\Phi) = 2.44 - 0.14 \cos(\Phi) \text{ \AA} \quad (7)$$

This enables to make direct connection between the measured supermodulation phase  $\Phi(\mathbf{r})$  obtained from the topographic image  $T(\mathbf{r})$  and the Cu-O separation  $\delta(\mathbf{r})$  within each crystal unit cell. Fig. 2 shows a typical example of the  $T(\mathbf{r}) : \Phi(\mathbf{r}) : \delta(\mathbf{r})$  arising from this procedure. SI Fig. 2 shows a typical example of the equivalent  $T(\mathbf{r}) : \Phi(\mathbf{r}) : \delta(\mathbf{r})$  arising from this procedure when using a  $\text{Bi}_2\text{Sr}_2\text{CaCu}_2\text{O}_{8+x}$  nanoflake tip for SJTM measurements of  $n_p(\mathbf{r})$ .

### (III) Charge Transfer Energy Visualization $\mathcal{E}(\mathbf{r})$ by SISTM

To extract the spatially resolved charge transfer energy  $\mathcal{E}(\mathbf{r})$ , high voltage<sup>8,9,10</sup> differential tunnel conductance  $g(\mathbf{r}, V)$  imaging of  $\text{Bi}_2\text{Sr}_2\text{CaCu}_2\text{O}_{8+x}$  is used. Here, we visualize  $g(\mathbf{r}, V)$  in the range  $-1.6 \text{ V} \leq V \leq 2 \text{ V}$  at junction resistance  $R_N \approx 85 \text{ G}\Omega$  ( $V_S = 600 \text{ mV}$ ;  $I_S = 7 \text{ pA}$ ). SI Fig. 3 shows a typical example of a  $g(\mathbf{r}, V)$  series measured at  $T=4.2\text{K}$  along a line transverse to the crystal supermodulation. The edges of the filled lower band and the empty upper band can be identified from the appearance of extremely rapid increase in the density of states (inset Fig. 3). The energy separation  $\mathcal{E}$  between these bands is estimated by measuring the energy range between these SI ges at a constant differential conductance  $G$ .

In our studies we choose to use  $G \approx 20 \text{ pS}$  for practical reasons explained below. However, the demonstration that the charge-transfer energy  $\mathcal{E}(\mathbf{r})$  varies periodically with the crystal supermodulation is not contingent on any specific value for  $G$ . Thus, SI Fig. 4 shows  $\mathcal{E}(G, \mathbf{r})$  maps extracted at selected values of  $G$  ranging from  $20 \text{ pS}$  to  $80 \text{ pS}$ . One can see that the spatial structure of  $\mathcal{E}(G, \mathbf{r})$  is extremely similar for  $20 \text{ pS} < G < 80 \text{ pS}$ . Moreover, the power spectral density Fourier transform  $\mathcal{E}(G, \mathbf{q})$  of every one exhibits strong peaks at wavevectors  $\pm \mathbf{Q}_S$ . This means that the relationship between  $\mathcal{E}$  and  $\Phi$  will be qualitatively the same for any  $G$  considered here, but with somewhat different amplitudes for  $\mathcal{E}$ .

There is, however, another difference between the  $\mathcal{E}(G, \mathbf{r})$  measured in the range  $40 \text{ pS} < G < 80 \text{ pS}$  and at  $G = 20 \text{ pS}$ . It is the presence of dark regions at each oxygen dopant ion where strong local maxima occur<sup>8</sup> in  $g(\mathbf{r}, V)$  at conductance higher than  $20 \text{ pS}$ , preventing accurate measurement of  $\mathcal{E}(\Phi)$ . To avoid this complication, we focus on analysis of the  $G = 20 \text{ pS}$  charge transfer energy maps. SI Fig. 5 (a-c) show  $\mathcal{E}(\mathbf{r})$

obtained by this procedure in three disjoint fields of view. Each has an area of  $19.5 \times 19.5 \text{ nm}^2$  and their  $\mathcal{E}(\mathbf{r})$  have extremely similar spatial structure, with spatially-averaged values  $\langle \mathcal{E} \rangle \approx 1.195 \text{ eV}, 1.205 \text{ eV}$  and  $1.215 \text{ eV}$  respectively. These average charge-transfer energies are in excellent quantitative agreement with those derived from a variety of experimental techniques, including SISTM<sup>4</sup>, ARPES<sup>5, 11</sup> and optical spectroscopy<sup>12</sup> of  $\text{Bi}_2\text{Sr}_2\text{CaCu}_2\text{O}_{8+x}$ . To further underscore the statistical validity of  $\mathcal{E}$ , SI Fig. 5 d,e,f show the phase-averaged, Fourier-filtered  $\mathcal{E}(\Phi)$  in the same three fields of view. It is readily apparent that the peak-to-peak amplitude is the same for all three fields of view, and  $\mathcal{E}(\Phi)$  is minimized at  $\Phi \approx \pi$  in all three fields of view.

#### (IV) Electron-pair Density Visualization $n_p(\mathbf{r})$ by SJTM

The macroscopic wavefunctions of the tip and sample forming a Josephson junction can be written as

$$\psi_T = \langle c_\uparrow c_\downarrow \rangle_T e^{-i\varphi_T} = \sqrt{n_T} e^{-i\varphi_T} \quad (8)$$

$$\psi_S = \langle c_\uparrow c_\downarrow \rangle_P e^{-i\varphi_S} = \sqrt{n_P} e^{-i\varphi_S} \quad (9)$$

where  $n_T$  ( $n_P$ ) and  $\varphi_T$  ( $\varphi_S$ ) are the electron-pair densities and the phases of the tip (sample), respectively. The product of the Josephson critical current  $I_J$  with the junction's normal-state resistance  $R_N$  is<sup>13</sup>:

$$I_J R_N \propto \langle c_\uparrow c_\downarrow \rangle_P \langle c_\uparrow c_\downarrow \rangle_T \propto \sqrt{n_P} \sqrt{n_T}. \quad (10)$$

Assuming  $n_T$  to be constant, the sample electron-pair density  $n_P$  can be measured as  $n_P \propto (I_J R_N)^2$ . In a phase-diffusive Josephson junction, the current - voltage  $I_P(V_J)$  characteristic is described by the following equation with the maximum Josephson current ( $I_m = \frac{I_J^2 Z}{4V_c}$ ) appearing at non-zero junction voltages  $V_c$ :

$$I_P(V_J) = \frac{1}{2} I_J^2 Z V_J / (V_J^2 + V_c^2) \quad (11)$$

Here,  $Z$  is the impedance relevant to re-trapping of the diffusing phase. The first derivative of  $I_P(V_J)$  at zero bias is

$$g_0 \equiv \left. \frac{dI_P}{dV_J} \right|_{V_J=0} = \frac{I_J^2 Z}{2V_c^2} \propto I_m \quad (12)$$

In scanned Josephson tunneling microscopy (SJTM) using superconductive STM tips, the sample electron-pair density can therefore be visualized<sup>14,15,16,17</sup> by measuring either



$I_m(\mathbf{r})$  or  $g_0(\mathbf{r})$  and, also separately measuring  $R_N^2(\mathbf{r})$  in the identical field of view yielding the electron-pair density as:

$$n_p(\mathbf{r}) \propto I_m R_N^2(\mathbf{r}) \propto g_0 R_N^2(\mathbf{r}). \quad (13)$$

For these studies, we use a  $\text{Bi}_2\text{Sr}_2\text{CaCu}_2\text{O}_{8+x}$  nanoflake tip<sup>15</sup>. A single crystal sample of  $\text{Bi}_2\text{Sr}_2\text{CaCu}_2\text{O}_{8+x}$  at the hole density  $p = 0.17 \pm 0.01$  and superconducting transition temperature  $T_c = 91$  K is cleaved in cryogenic ultra-high vacuum. The nanoflake tip is then created by picking up a nanometer scale  $\text{Bi}_2\text{Sr}_2\text{CaCu}_2\text{O}_{8+x}$  flake from the sample surface. A typical resulting topography is shown in SI Fig. 2 in which both the locations of individual Bi atoms at the BiO termination layer and the crystal supermodulation are all well resolved<sup>6,18</sup>.

To extract the phase-diffusive Josephson differential conductance at zero bias  $g_0$  from  $g(V_j, \mathbf{r})$  we fit this Josephson junction differential conductance spectrum to the 1<sup>st</sup> derivative of Eq. (11) with free fitting parameters being  $\frac{1}{2}I_J^2 Z$ ,  $V_c$  and an additional constant  $C$  added to take account of any small conductance offsets that may occur systematically, and from which fits the  $g_0(\mathbf{r})$  and  $I_m(\mathbf{r})$  are derived.

SI Fig 10 shows a linecut of  $I_m$  along the  $q = \mathbf{Q}_{SM}$  direction, normalized to the background value  $I_m(\mathbf{q} = \mathbf{0})$  for three different experiments in three different fields of view along with the equivalent linecut for  $g_0$  used to generate Fig. 5. The consistency in the amplitude of supermodulation in  $I_m$  and  $g_0$  across the various experiments demonstrates the repeatability of the superfluid density modulation measurements.

## (V) Determination of Equivalent Normal State Junction Resistance $R_N$

The Josephson tunnel junction resistance  $R_N(\mathbf{r})$  is difficult to determine in a single  $g(\mathbf{r}, V)$  map because  $I_P(V_j)$  is measured in the  $\mu\text{V}$  range (Fig. 3b), whereas  $R_N(\mathbf{r})$  is only quantifiable using differential conductance measurements at the 100 mV range (at  $E \gg \Delta_{SIS}$  where for cuprates  $\Delta_{SIS} > 50\text{meV}$ ). Thus we use a two-step procedure in which we measure a low voltage range  $g_1(\mathbf{r}, V)$  and a high voltage range  $g_2(\mathbf{r}, V)$  in exactly the same FOV (SI Fig. 6). The  $g_1(\mathbf{r}, V)$  ranges from  $-15 \text{ mV} < V < 15 \text{ mV}$  with a setpoint

$I_{s1} = 100 \text{ pA}$ ,  $V_{s1} = 15 \text{ mV}$ , while  $g_2(\mathbf{r}, V)$  is acquired from  $-350 \text{ mV} < V < 350 \text{ mV}$  in the almost identical FOV at setpoint  $I_{s2} = 350 \text{ pA}$ ,  $V_{s2} = 350 \text{ mV}$  so that  $V_{s2} \gg \Delta_{SIS}$ .

Thus,  $g_1(\mathbf{r}, V)$  and  $g_2(\mathbf{r}, V)$  are obtained in different measurements but nominally the same field of view (FOV). These images, along with their associated topographs  $T(\mathbf{r})$ , are then registered to the exact same FOV by a series of transformations. Each experimental image  $T(\mathbf{r})$  can be registered to the expected periodic lattice using the Lawlor-Fujita (LF) procedure<sup>19</sup>, which utilizes a 2D lock-in method to solve for the displacement field  $\mathbf{r} - \tilde{\mathbf{r}}$  between the experimentally measured  $T(\mathbf{r})$  and a perfectly lattice periodic map  $T^0(\mathbf{r})$ . After this procedure, the lattice is almost exactly periodic, but can sometimes still be sheared such that the expected  $C4$  symmetry of the lattice is not satisfied. To correct this, we apply a shear transformation to the experimental data. Once the experimental images have been corrected, they are then atomically registered to the perfectly identical FOV by rigidly shifting the maps relative to one another. After this procedure,  $g_1(\mathbf{r}, V)$  and  $g_2(\mathbf{r}, V)$  are now in a precisely identical FOV.

The  $g_1(\mathbf{r}, V_J)$  is then fit with a parabolic curve  $g_1 = a_1 V_J^2 + b_1$  over the voltage range  $[-V_{s1}, V_{s1}]$  at every  $\mathbf{r}$ . A small energy range within which Josephson electron-pair tunneling dominates surrounding  $V_J = 0$  is omitted. Next  $g_2(\mathbf{r}, V_J)$  is smoothed and fit with a parabolic curve  $g_2 = a_2 V_J^2 + b_2$  over a voltage range  $[-V_0, V_0]$ , where  $V_{s1} < V_0 < \Delta_{SIS}$ . Finally, we determine the scaling factors between  $g_2(\mathbf{r})$  and  $g_1(\mathbf{r})$  via  $g_1(\mathbf{r}) = g'_2(\mathbf{r}) = \alpha(\mathbf{r})g_2(\mathbf{r}) + \beta(\mathbf{r})$ , where  $\alpha = \frac{a_1}{a_2}$ ,  $\beta = b_1 - b_2 \frac{a_1}{a_2}$ .

$$g'_2(\mathbf{r}, V_J) = \alpha(\mathbf{r})g_2(\mathbf{r}, V_J) + \beta(\mathbf{r}). \quad (14)$$

The rescaled  $g'_2(V_J)$  and the original  $g_1(V_J)$  when plotted on the same graph are now virtually indistinguishable (SI Fig. 6c), and the high-voltage conductance  $g'_2(\mathbf{r}, V_J)$  associated with the junction resistance  $R_N$  for the conditions of Josephson tunneling be read off for each  $\mathbf{r}$ . The rescaled  $g'_2(\mathbf{r}, V)$  and the original  $g_1(\mathbf{r}, V)$  images are shown in SI Fig. 7 demonstrating the fidelity of the rescaling process. Finally, we can establish the normal state junction resistance corresponding to the low-voltage  $g_1(\mathbf{r}, V_J)$  map:

$$R_N(\mathbf{r}) \equiv \frac{1}{g'_2(\mathbf{r}, V_{s2})}. \quad (15)$$

A typical example of such data  $R_N(\mathbf{r})$  which is used to establish  $n_p(\mathbf{r}) \propto g_0 R_N^2(\mathbf{r})$  as in Figs 4,5 is shown in **SI** Fig. 8.

### (VI) Determination of the Relationships $\tilde{\mathcal{E}}(\Phi)$ and $\tilde{n}_p(\Phi)$

To measure the dependence of charge transfer energy modulations  $\mathcal{E}(\Phi)$  and electron – pair density modulations  $n_p(\Phi)$  on the supermodulation phase  $\Phi$ , the first step is to Fourier filter the quantity of interest  $A(\mathbf{r})$ , either  $\mathcal{E}(\mathbf{r})$  or  $n_p(\mathbf{r})$ , retaining only contributions from the wavevectors close to  $\mathbf{q} = \pm \mathbf{Q}_S$  and adding the constant background  $\langle A \rangle$ :

$$\tilde{A}(\mathbf{r}) = \langle A \rangle + \frac{1}{\sigma\sqrt{2\pi}} \int A(\mathbf{q}) e^{-i\mathbf{q}\cdot\mathbf{r}} \left( e^{\frac{|\mathbf{q}-\mathbf{Q}_S|^2}{2\sigma^2}} + e^{\frac{|\mathbf{q}+\mathbf{Q}_S|^2}{2\sigma^2}} \right) d\mathbf{q}. \quad (16)$$

Next, we calculate the supermodulation phase  $\Phi(\mathbf{r})$  from the topograph  $T(\mathbf{r})$  in the same FOV as  $A(\mathbf{r})$ . We then bin each pixel in the FOV according to its local phase  $\Phi(\mathbf{r})$ . Since each pixel is associated with a pair  $(\tilde{A}(\mathbf{r}), \Phi(\mathbf{r}))$ , this yields a two-dimensional histogram showing the coincidence of these values. This is shown for  $\tilde{\mathcal{E}}(\mathbf{r})$  and  $\tilde{n}_p(\mathbf{r})$  in SI Fig. 9 a and c, which are the core empirical data for this project. The ultimate step is to average  $\tilde{A}(\mathbf{r})$  for every  $\mathbf{r}$  with a given value of  $\Phi$  yielding the plot  $\tilde{A}(\Phi)$  as shown for  $\tilde{\mathcal{E}}(\mathbf{r})$  and  $\tilde{n}_p(\mathbf{r})$  in SI Fig. 9b, d.

For  $\text{Bi}_2\text{Sr}_2\text{CaCu}_2\text{O}_{8+x}$  a similar procedure has been used to plot the energy gap for single-particle excitations  $\Delta(\Phi)$  as a function of phase<sup>20</sup>. The results are that  $\Delta$  is also modulated at  $\mathbf{Q}_S$  and that its value is minimized at  $\Phi \approx \pi$ . Therefore, the data in Fig. 5 imply  $\Delta$  and  $n_p$  are out of phase by  $\pi$  for  $\text{Bi}_2\text{Sr}_2\text{CaCu}_2\text{O}_{8+x}$ . This is as would be expected in a strongly correlated unconventional superconductor described by the Hubbard model such as Eqn. 1. In that case, it is well known that the gap to single-particle excitations evolves oppositely<sup>21,22</sup> with hole-density  $p$  to the amplitude of the coherent electron-pair wavefunction  $\Psi$ .

### (VII) Estimation of $\alpha$ from Three-band $\text{CuO}_2$ Hubbard Model Calculations

Theoretical calculations of  $\Psi$  and  $\mathcal{E}$  have been carried out by numerical solution of the Emery three-band model within the framework of cluster dynamical mean field theory (CDMFT). One can extract predicted values of  $\alpha = dn_p/d\mathcal{E}$  for comparison with

the experimental results in Fig. 5d. Here the measured  $g_0 R_N^2$  is proportional to  $n_p$ , but the constants of proportionality are unknown so one we cannot (yet) compare this quantity to  $n_p = |\Psi|^2$  calculated using CDMFT in absolute units. Thus, one needs to normalize both the experimental results and the theoretical predictions in a consistent manner.

To do so, we first normalize measured  $g_0 R_N^2$  to its mean value in the experimental FOV:

$$\bar{n}_p = \frac{g_0 R_N^2}{\langle g_0 R_N^2 \rangle} \quad (17)$$

as shown in Fig. 5. The CDMFT calculated  $|\Psi|$  in Ref. 23 is normalized to the reference value of  $|\Psi|$  for the so-called covalent case  $|\Psi|_{\text{cov}} = 0.0774$ , whose input material parameters are chosen to be representative of  $\text{Bi}_2\text{Sr}_2\text{CaCu}_2\text{O}_{8+x}$ .

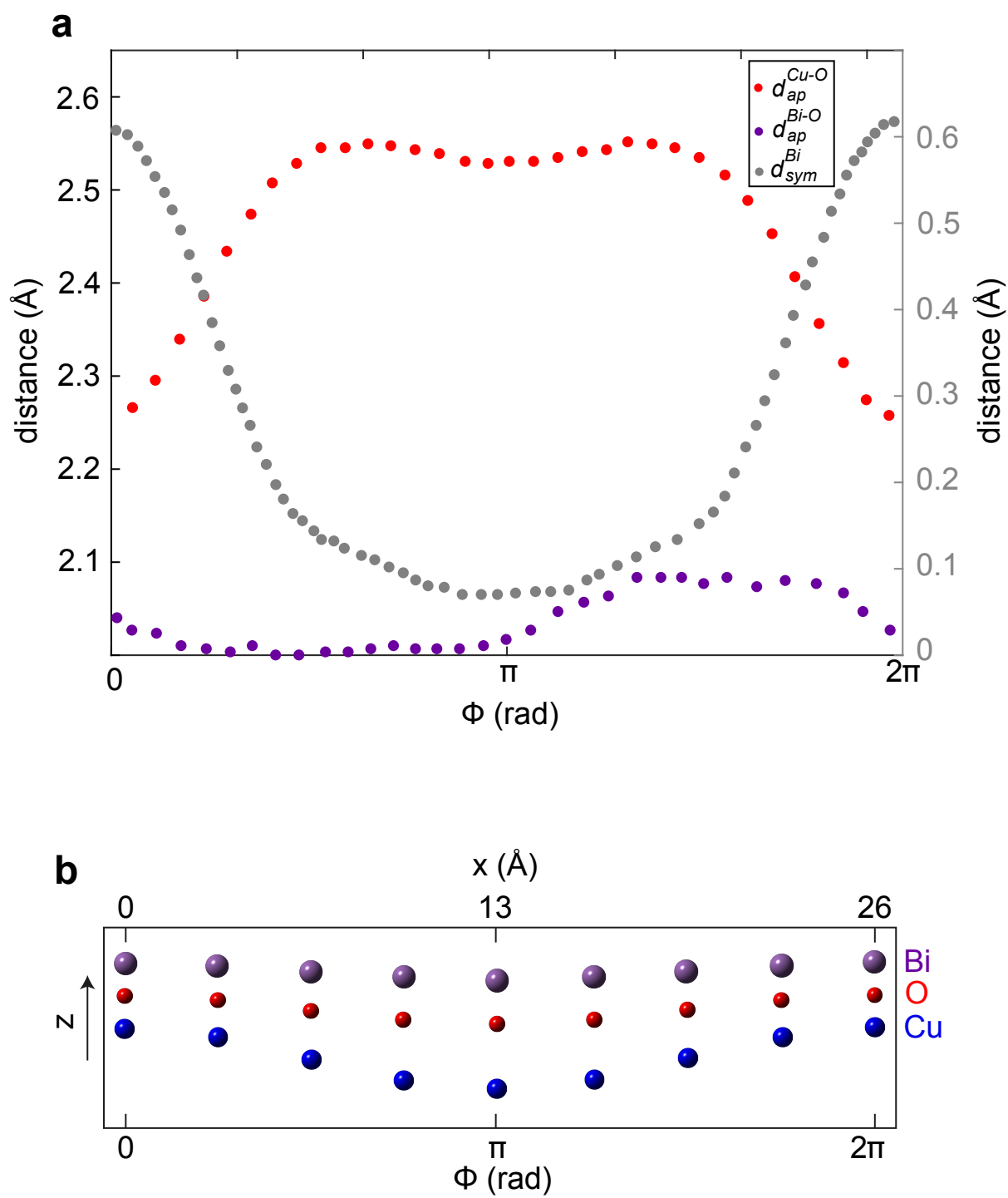
$$|\overline{c_\uparrow c_\downarrow}|^{\text{BSCCO}} = \frac{|\Psi|}{|\Psi|_{\text{cov}}} \quad (18)$$

Normalization of results for  $\text{La}_2\text{CuO}_4$  in Ref. 24 is achieved similarly as

$$|\overline{c_\uparrow c_\downarrow}|^{\text{LSCO}} = \frac{|\Psi|}{|\Psi|_{\text{LSCO}}}, \quad (19)$$

where  $|\Psi|_{\text{LSCO}} = 0.0154$ . Since  $\text{Bi}_2\text{Sr}_2\text{CaCu}_2\text{O}_{8+x}$  is among the cuprates with the smallest value of  $\mathcal{E}$  and  $\text{La}_2\text{CuO}_4$  is among those with the largest, we define a range of  $\alpha$  for the cuprates ranging between the values of Ref. 24 and Ref. 25 to arrive at the inequality  $0.3 \lesssim \alpha \lesssim 1.0 \text{ eV}^{-1}$ . This is represented by the yellow shaded wedge in Fig. 5d. The measured value of  $\alpha = -0.81 \pm 0.17 \text{ eV}^{-1}$  falls in this range and very close to the DMFT prediction for  $\text{Bi}_2\text{Sr}_2\text{CaCu}_2\text{O}_{8+x}$ .

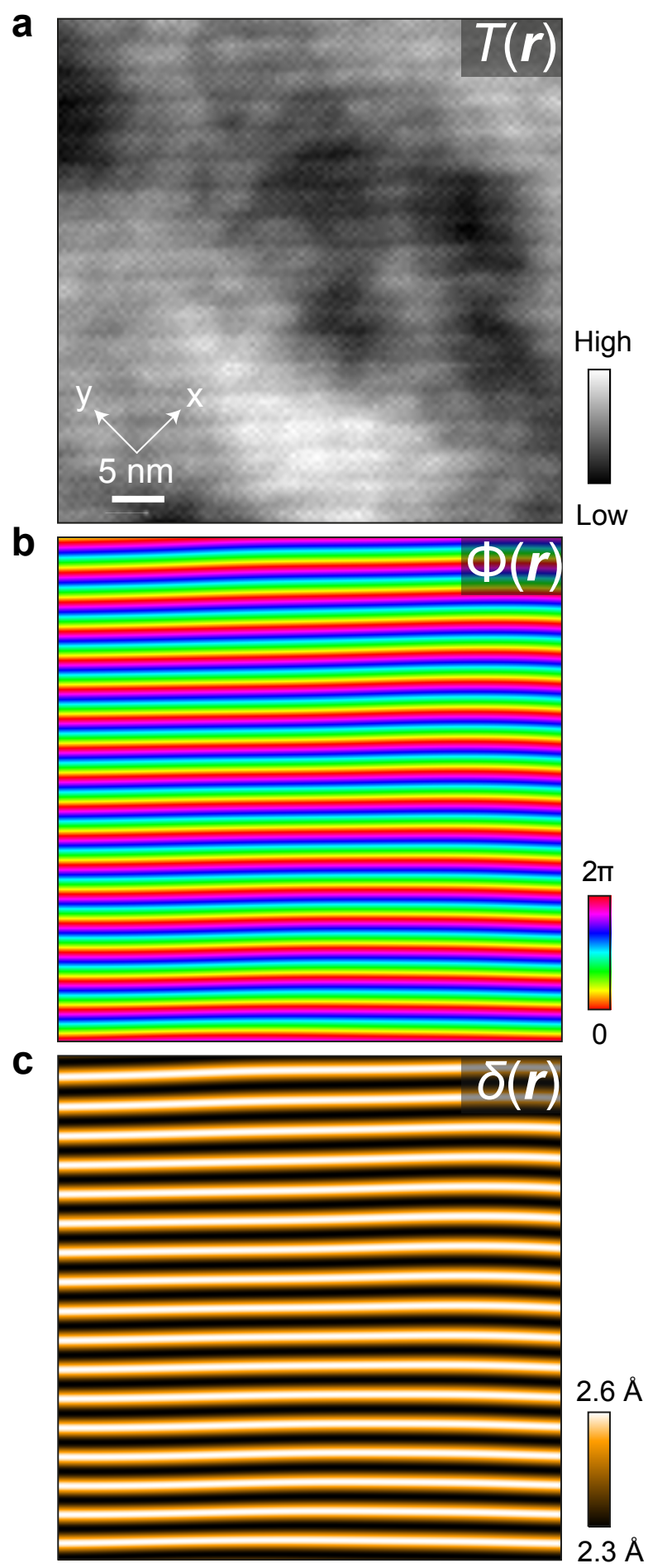
SI FIG 1



### SI Figure 1: $\text{Bi}_2\text{Sr}_2\text{CaCu}_2\text{O}_{8+x}$ Crystal Supermodulation

- a. Left hand axis: apical Cu-O and Bi-O distances as a function of supermodulation phase  $\phi$  from Ref. 7. Right hand axis: displacement of Bi-O termination layer from symmetry plane of crystal as a function of supermodulation phase  $\phi$  from X-ray data<sup>7</sup>. The latter measures the same quantity as the STM topograph  $T(\mathbf{r})$  enabling one to form a one-to-one mapping between the supermodulation phase  $\phi$  we extract from  $T(\mathbf{r})$  and the phase variable in the X-ray refinement. Further, the relatively small amplitude of Bi-O modulation compared to the Cu-O apical modulation enables one to make a direct connection between  $\phi$  and  $\delta$ .
- b. Schematic showing the atomic modulations induced along the  $z$  axis by the supermodulation. The  $\text{CuO}_2$  layer modulates with a larger amplitude than the SrO layer, resulting in  $\delta$  being maximal at  $\phi = \pi$ , where the topograph elevation has its minimum.

SI FIG 2

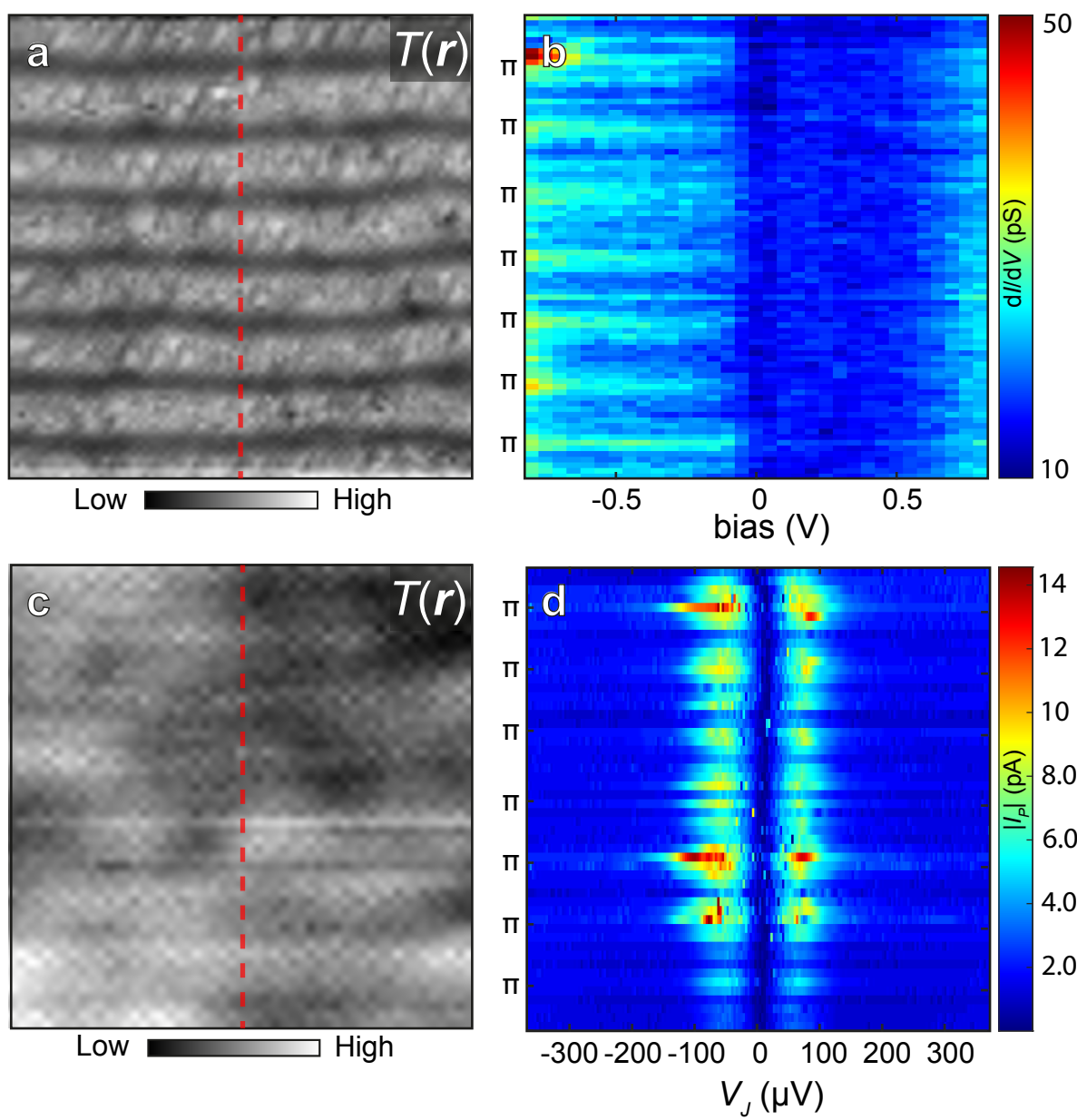


## SI Figure 2: Bi<sub>2</sub>Sr<sub>2</sub>CaCu<sub>2</sub>O<sub>8+x</sub> Nanoflake Topography

Evaluation of a:  $T(\mathbf{r})$ , b:  $\Phi(\mathbf{r})$  and c:  $\delta(\mathbf{r})$  when using the Bi<sub>2</sub>Sr<sub>2</sub>CaCu<sub>2</sub>O<sub>8+x</sub> nanoflake tip<sup>14,17</sup>. The atomic structure of the Bi-O termination layer and the supermodulation are clearly visible in  $T(\mathbf{r})$ . The supermodulation phase can be readily extracted from the total  $T(\mathbf{r})$  signal and is related to  $\delta(\mathbf{r})$  through the fitting in Eq. 7.



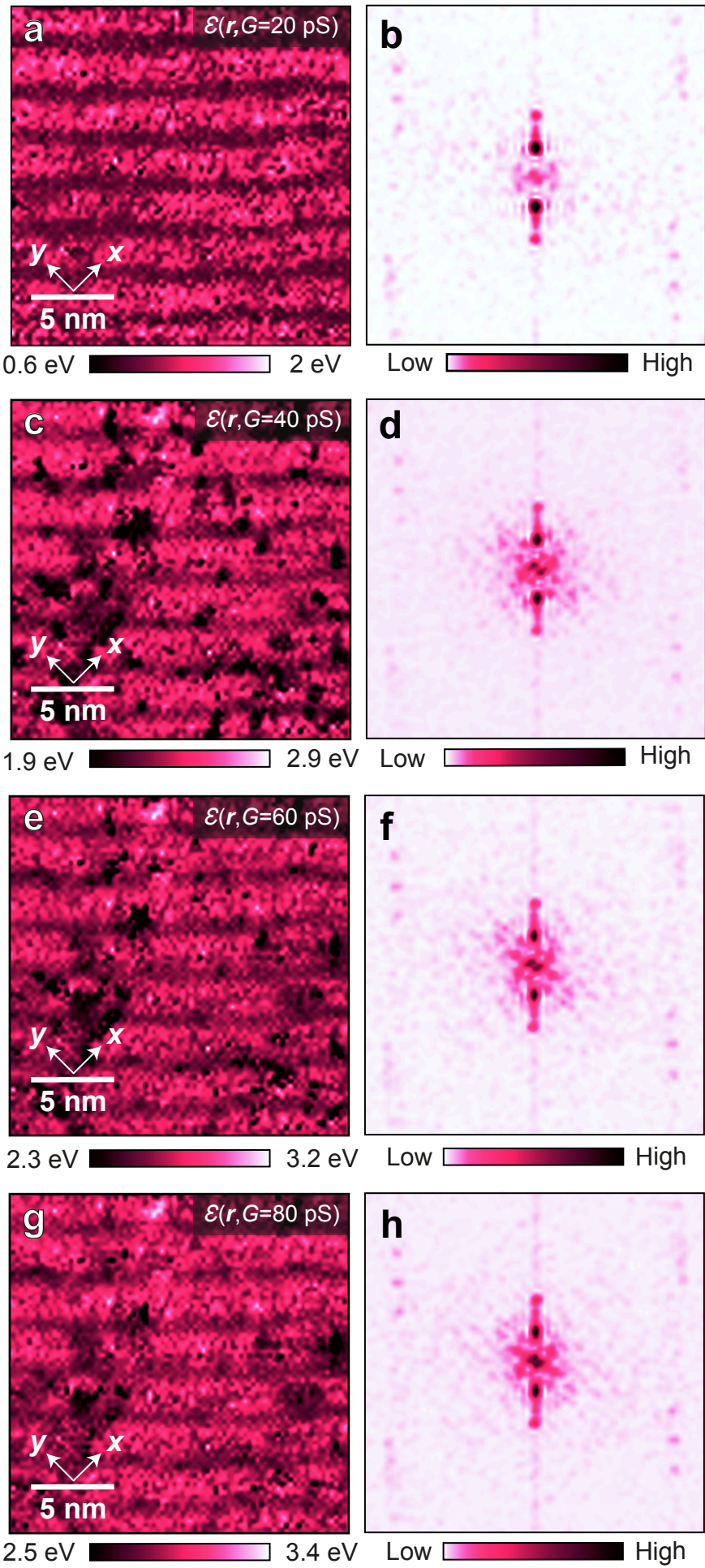
SI FIG 3



**SI Figure 3: Periodic Modulations in High-Voltage  $g(\mathbf{r}, V)$  and Low-Voltage  $I_m(\mathbf{r}, V)$**

- a.  $T(\mathbf{r})$  showing tip-trajectory along a direction perpendicular to the supermodulation as a red dashed line.
- b. Spectrogram of  $g(\mathbf{r}, V)$  along the trajectory indicated by the red dashed line in a. Modulations of the upper and lower bands are clearly visible.
- c.  $T(\mathbf{r})$  showing tip-trajectory along a direction perpendicular to the supermodulation as a red dashed line.
- d. Spectrogram of a typical  $I_p(\mathbf{r}, V)$  measured at 45 mK along the trajectory indicated by the red dashed line in c. Modulations of the positive and negative peaks are clearly visible.

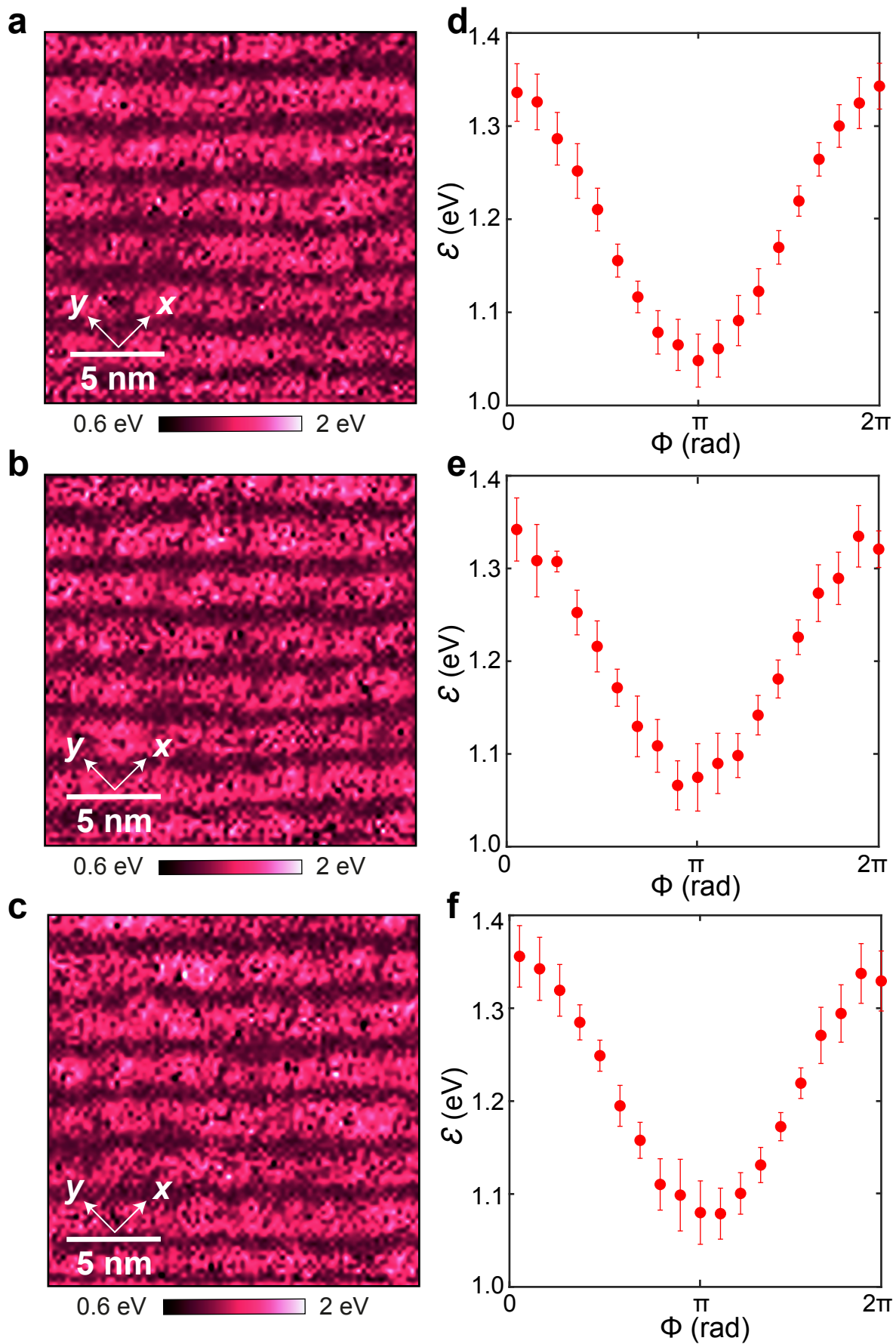
SI FIG 4



**SI Figure 4: Imaging  $\mathcal{E}(G, r)$  in Different  $G$** 

Calculated  $\mathcal{E}(G, r)$  for input differential conductance  $G$  of a: 20 pS, c: 40 pS, e: 60 pS and g: 80 pS showing that the spatial structure of  $\mathcal{E}$  is relatively insensitive to our choice of  $G$ , apart from the presence of Oxygen dopant peaks at  $G \geq 40$  pS. Panels b, d, f and h show the corresponding power spectral densities, which have clear peaks at  $q \approx \pm Q_S$  for all values  $G$  considered.

SI FIG 5



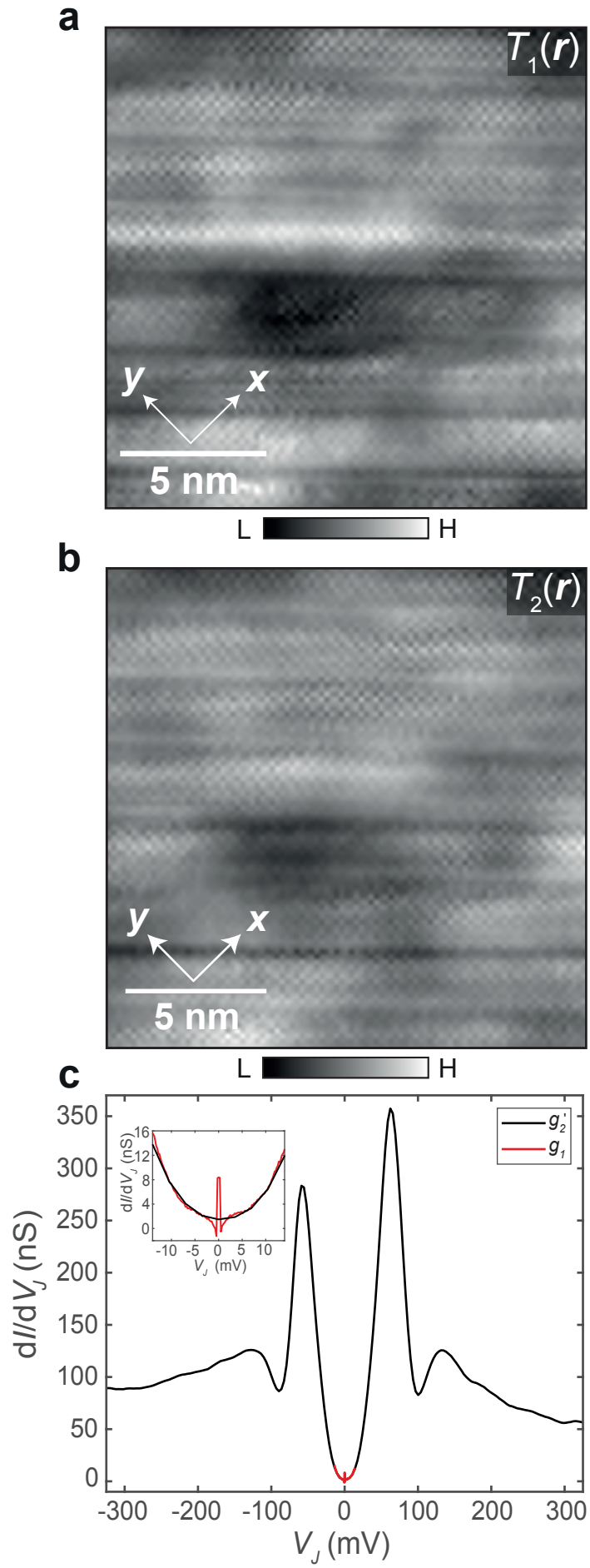
**SI Figure 5: Imaging  $\mathcal{E}(\mathbf{r})$  in Different Fields of View.**

(a-c)  $\mathcal{E}(\mathbf{r})$  calculated in 3 disjoint  $19.5 \times 19.5 \text{ nm}^2$  fields of view.

(d-f) Phase-averaged  $\tilde{\mathcal{E}}(\phi)$  calculated in 3 disjoint  $19.5 \times 19.5 \text{ nm}^2$  fields of view.

$\tilde{\mathcal{E}}(\phi)$  is peaked at  $\phi \approx \pi$  with a peak-to-peak amplitude of  $\sim 0.3 \text{ eV}$  in all three fields of view.

SI FIG 6





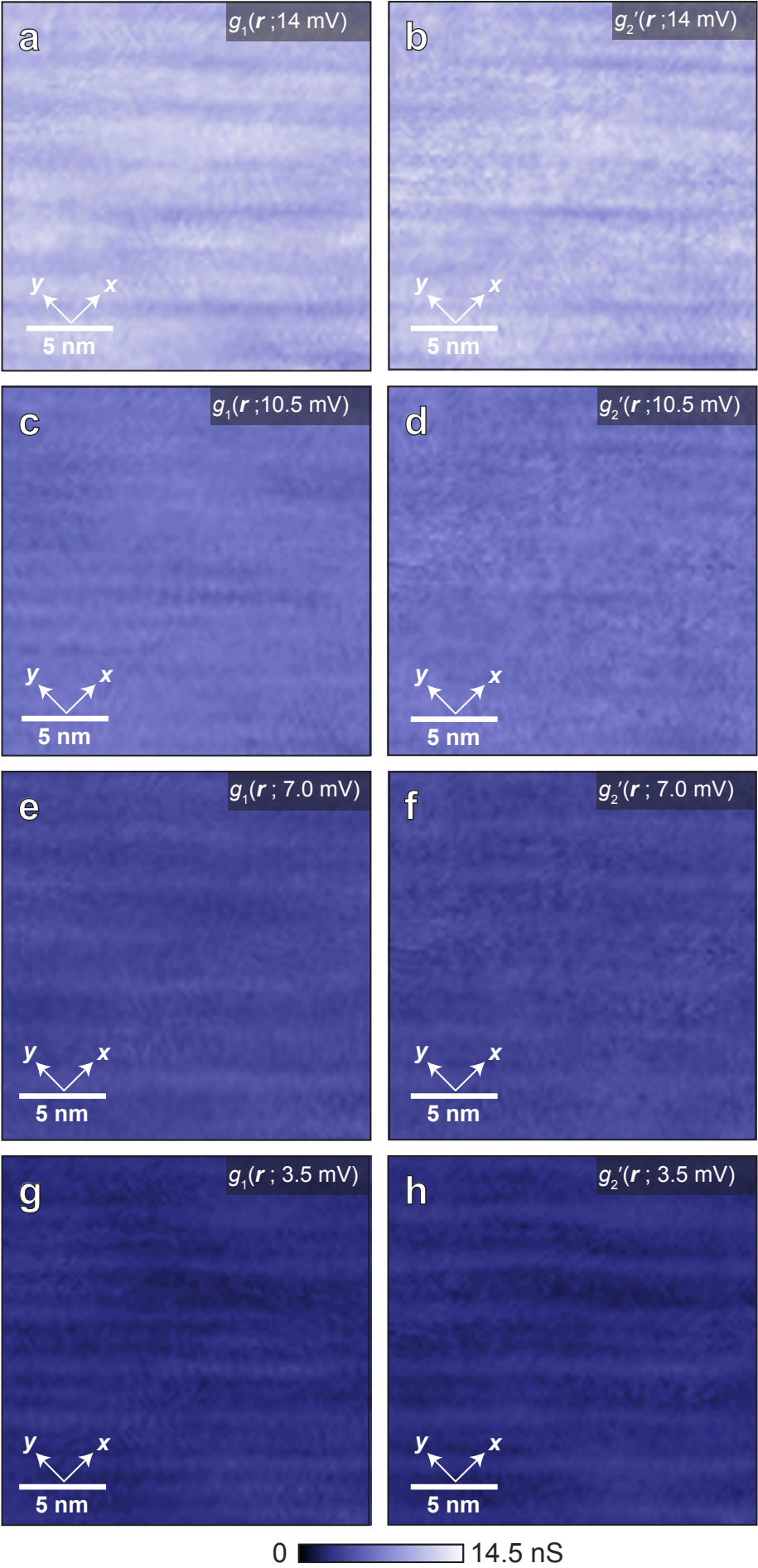
**SI Figure 6: Scaling High-Voltage and Low-Voltage  $g(\mathbf{r}, V_J)$  for  $R_N(\mathbf{r})$**

(a-b) Simultaneous topographies of  $g_1(\mathbf{r}, V_J)$  and  $g_2(\mathbf{r}, V_J)$  .

c. Typical example of a rescaled  $g'_2(V_J)$  and the original  $g_1(V_J)$  spectra. Inset: Same spectra plotted for voltages in the range  $-V_{s1} \leq V_J \leq V_{s1}$ .



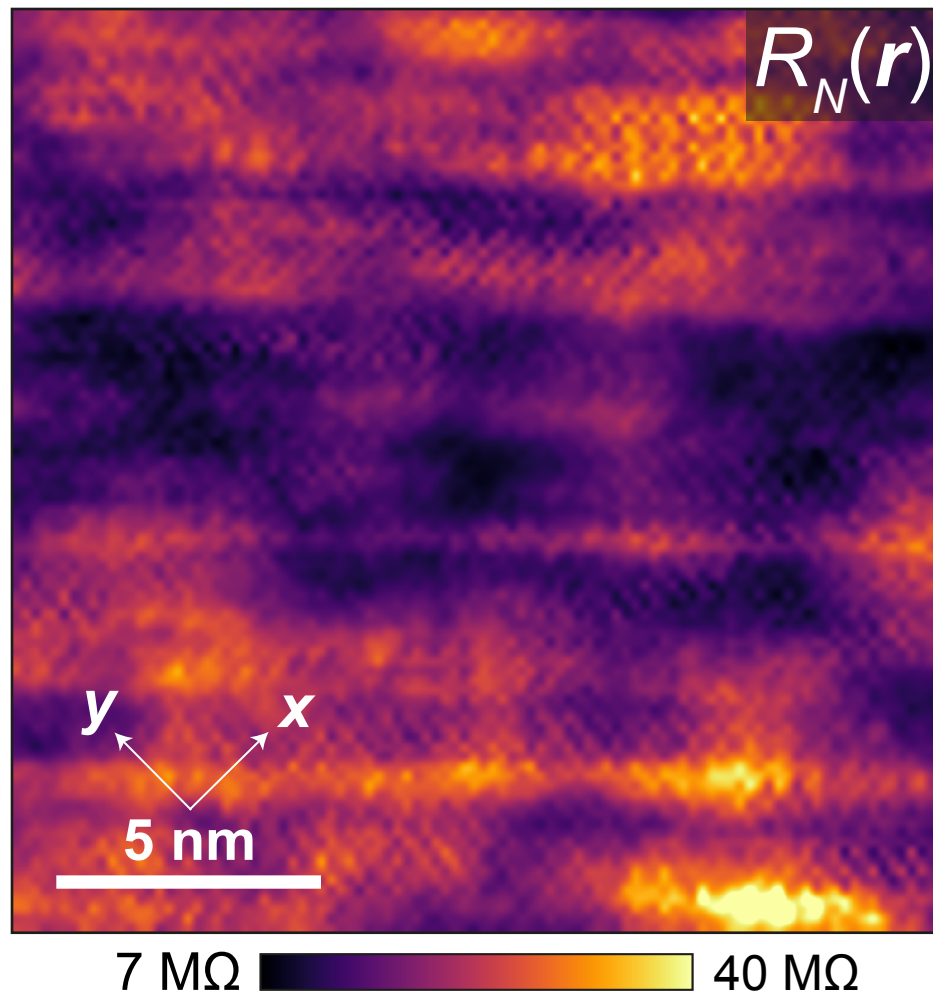
SI FIG 7



**SI Figure 7: Rescaled  $g(\mathbf{r}, V)$  Images**

(a-h) The rescaled  $g'_2(\mathbf{r}, V)$  and original  $g_1(\mathbf{r}, V)$  images compared at voltages ranging from 3.5 mV to 14 mV. They are virtually identical, validating the scaling procedure used to obtain  $R_N(\mathbf{r})$ .

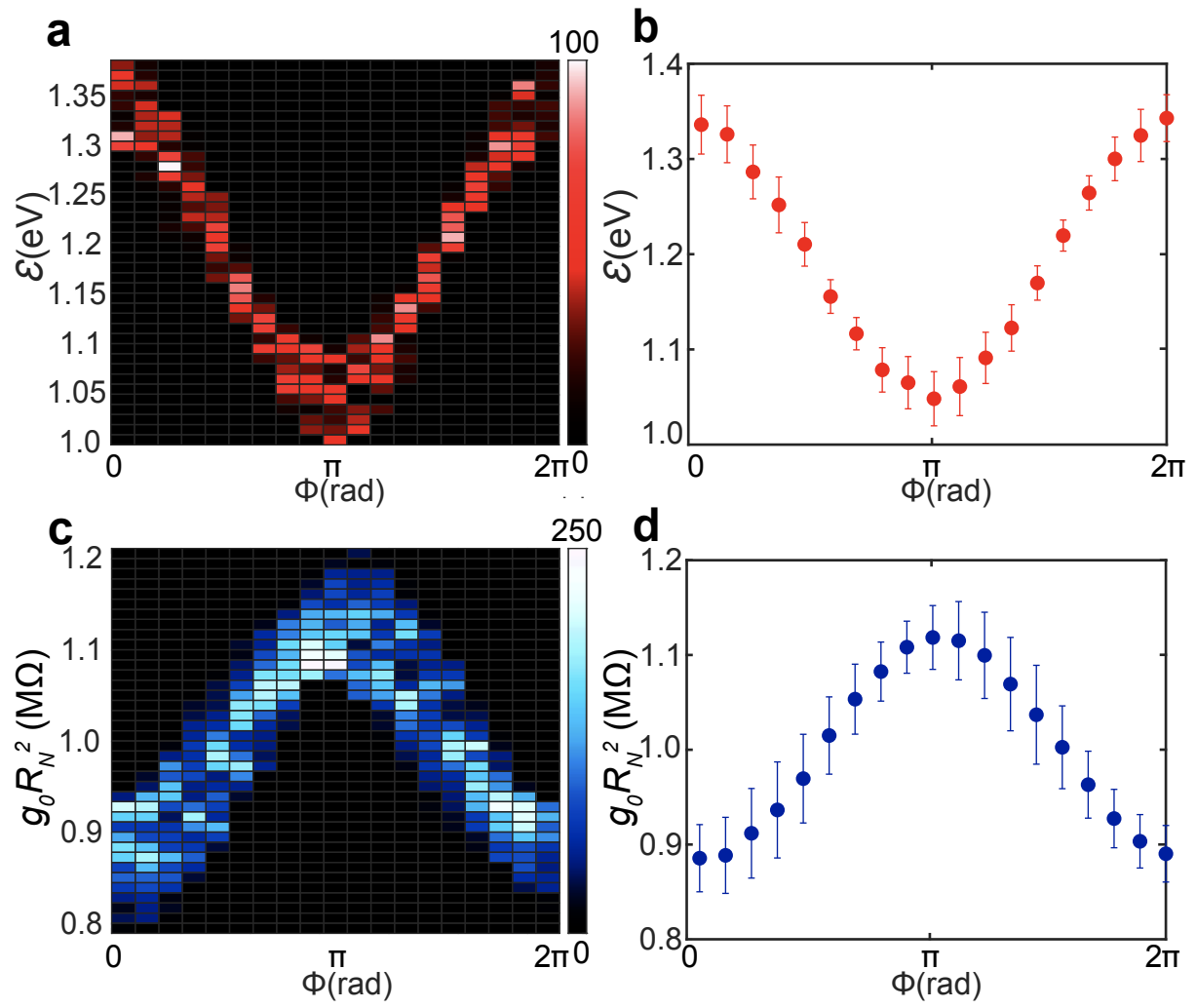
SI FIG 8



**SI Figure 8: Imaging  $R_N(\mathbf{r})$** 

Image of the normal-state junction resistance  $R_N(\mathbf{r}) \equiv 1/g'_2(\mathbf{r}, V_{s2})$  at which the  $g_1(\mathbf{r}, V_J)$  map was measured.

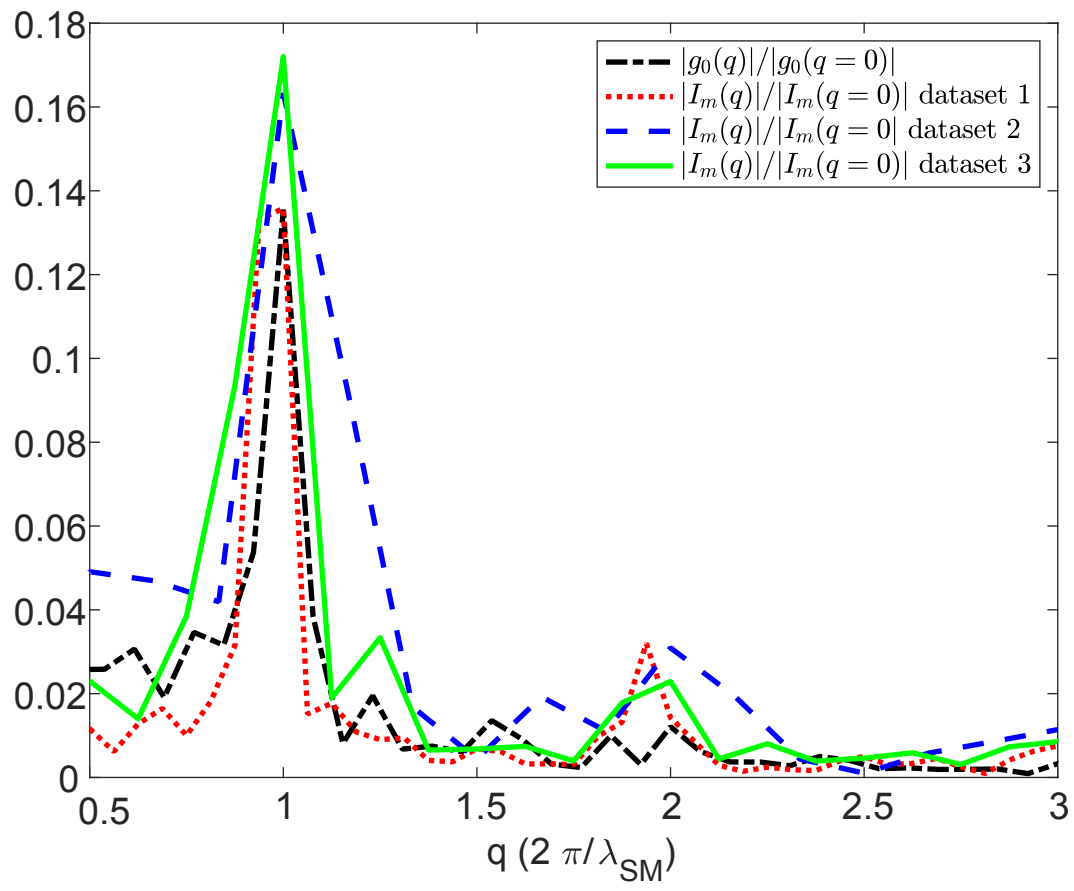
SI FIG 9



**SI Figure 9: Determining  $\tilde{\mathcal{E}}(\Phi)$  and  $\tilde{n}_p(\Phi)$**

- a. Two-dimensional histogram of  $\tilde{\mathcal{E}}$  vs  $\Phi$ , clearly showing a minimum at  $\Phi \approx \pi$ .
- b.  $\tilde{\mathcal{E}}(\Phi)$  obtained by averaging  $\tilde{\mathcal{E}}$  within each phase bin.
- c. Two-dimensional histogram of  $\tilde{n}_p \propto g_0(\mathbf{r})R_N^2(\mathbf{r})$  vs  $\Phi$ , clearly showing a maximum at  $\Phi \approx \pi$ .
- d.  $\tilde{n}_p(\Phi) \propto g_0R_N^2(\Phi)$  obtained by averaging  $\tilde{n}_p$  within each phase bin.

SI FIG 10



**SI Figure 10: Repeatability of  $I_m$  Supermodulation Amplitude**

Fourier transform linecuts of  $I_m$  from three different experiments in three different fields of view along with the equivalent linecut for  $g_0$ . The black dashed curve corresponds to the  $g_0$  data used to compute superfluid density in the main text.



## References

---

- 1 Tokura, Y. et al. Cu-O network dependence of optical charge-transfer gaps and spin-pair excitations in single-CuO<sub>2</sub>-layer compounds. *Phys. Rev. B* **41**, 11657(R) (1990)
- 2 Cooper, S.L. et al. Optical studies of gap, exchange, and hopping energies in the insulating cuprates. *Phys. Rev. B* **42**, 10785(R) (1990)
- 3 Aronson, M. et al. Pressure dependence of the superexchange interaction in antiferromagnetic La<sub>2</sub>CuO<sub>4</sub>. *Phys Rev B* **44**, 4657 (1991)
- 4 Ruan, W. et al. Relationship between the parent charge transfer gap and maximum transition temperature in cuprates. *Sci. Bull.* **61**, 1826-1832 (2016)
- 5 Yang, S.-L. et al. Revealing the Coulomb interaction strength in a cuprate superconductor. *Phys Rev B* **96**, 245112 (2017)
- 6 Peng, Y.Y. et al. Influence of apical oxygen on the extent of in-plane exchange interaction in cuprate superconductors. *Nat. Phys.* **13**, 1201-1206 (2017)
- 7 Grebille, D., Leligny, H., Ruyter, A., Labbé, P. & Raveau, B. Static Disorder in the Incommensurate Structure of the High T<sub>c</sub> Superconductor Bi<sub>2</sub>Sr<sub>2</sub>CaCu<sub>2</sub>O<sub>8+δ</sub>. *Acta Crystallogr. Sect. B Struct. Sci.* **52**, 628–642 (1996).
- 8 McElroy, K., Lee, J., Slezak, J., Lee, D.-H., Eisaki, H., Uchida, S. & Davis, J.C. Atomic-scale sources and mechanism of the nanoscale electronic disorder in Bi<sub>2</sub>Sr<sub>2</sub>CaCu<sub>2</sub>O<sub>8+δ</sub>. *Science* **309**, 1048-1052 (2005).
- 9 Kohsaka, Y., Hanaguri, T., Azuma, M. et al. Visualization of the emergence of the pseudogap state and the evolution to superconductivity in a lightly hole-doped Mott insulator. *Nat. Phys.* **8**, 534-538 (2012).
- 10 Cai, P., Ruan, W., Peng, Y. et al. Visualizing the evolution from the Mott insulator to a charge-ordered insulator in lightly doped cuprates. *Nat. Phys.* **12**, 1047–1051 (2016)
- 11 Yang, S.-L. et al. Revealing the Coulomb interaction strength in a cuprate superconductor. *Phys Rev B* **96**, 245112 (2017)
- 12 Itoh, T., Fueki, K., Tanaka, Y. & Ihara, H. Optical conductivity spectra and electronic structure of Bi<sub>2</sub>Sr<sub>2</sub>(Y<sub>1-x</sub>Ca<sub>x</sub>)Cu<sub>2</sub>O<sub>y</sub> system *J. Phys. Chem. Solids* **60**, 41-51 (1999)
- 13 Kimura, H., Barber, Jr., R. P., Ono, S., Ando, Y. & Rynes, R. C. Josephson scanning tunneling

- 
- microscopy: A local and direct probe of the superconducting order parameter. *Phys. Rev. B* **80**, 144506 (2009)
- 14 Kimura, H., Barber Jr, R.P., Ono, S., Ando, Y., Dynes, R.C., Scanning Josephson tunneling microscopy of single-crystal  $\text{Bi}_2\text{Sr}_2\text{CaCu}_2\text{O}_{8+\delta}$  with a conventional superconducting tip. *Phys. Rev. Lett.* **101**, 037002 (2008).
  - 15 Hamidian, M., Edkins, S., Joo, S. et al. Detection of a Cooper-pair density wave in  $\text{Bi}_2\text{Sr}_2\text{CaCu}_2\text{O}_{8+x}$ . *Nature* **532**, 343-347 (2016).
  - 16 Cho, D., Bastiaans, K.M., Chatzopoulos, D. et al. A strongly inhomogeneous superfluid in an iron-based superconductor. *Nature* **571**, 541-545 (2019).
  - 17 Liu, X., Chong, Y. X., Sharma, R. & Davis, J. C. Discovery of a Cooper-pair density wave state in a transition-metal dichalcogenide. *arXiv:2007.15228*
  - 18 Du, Z., Li, H., Joo, S.H. et al. Imaging the energy gap modulations of the cuprate pair-density-wave state. *Nature* **580**, 65-70 (2020)
  - 19 Lawler, M. J., Fujita, K., Lee, J., Schmidt, A. R., Kohsaka, Y., Kim, C.K., Eisaki, H., Uchida, S., Davis, J. C., Sethna, J. P. & Kim, E. – A., Intra-unit-cell electronic nematicity of the high- $T_c$  copper-oxide pseudogap states. *Nature* **466**, 347 – 351 (2010).
  - 20 Slezak, J.A., Lee J., Wang, M. et al., Imaging the impact on cuprate superconductivity of varying the interatomic distances within individual crystal unit cells. *PNAS* **105**, 9, 3203-3208 (2008).
  - 21 Anderson, P.W. et al. The physics behind high-temperature superconducting cuprates: the 'plain vanilla' version of RVB. *J. Phys.: Condens. Matter* **16**, R755 (2004)
  - 22 Lee, P.A., Nagaosa, N. & Wen, X.-G. Doping a Mott insulator: Physics of high-temperature superconductivity. *Rev. Mod. Phys.* **78**, 17 (2006)
  - 23 Kowalski N., Dash S., Sénéchal D., Tremblay A. -M. S. Oxygen hole content, charge-transfer gap, covalency, and cuprate superconductivity *arXiv:2104.07087* (2021)
  - 24 Weber, C., Yee, C., Haule, K. & Kotliar, G. Scaling of the transition temperature of hole-doped cuprate superconductors with the charge-transfer energy. *Europhys. Lett.* **100**, 37001 (2012)